2023

Activity and stability of TiO2-encapsulated CsPbBr3/Cs4PbBr6 for photocatalytic degradation of Rhodamine B

Nutzeya Plainoen
Faculty of Engineering

Recommended Citation

Plainoen, Nutzeya, "Activity and stability of TiO2-encapsulated CsPbBr3/Cs4PbBr6 for photocatalytic degradation of Rhodamine B" (2023). *Chulalongkorn University Theses and Dissertations (Chula ETD)*. 10207.
https://digital.car.chula.ac.th/chulaetd/10207

Activity and stability of TiO_2-encapsulated $CsPbBr_3$/Cs_4PbBr_6 for photocatalytic degradation of Rhodamine B

Miss Nutzeya Plainoen

A Thesis Submitted in Partial Fulfillment of the Requirements
for the Degree of Master of Engineering in Chemical Engineering
Department of Chemical Engineering
Faculty Of Engineering
Chulalongkorn University
Academic Year 2023

การเกิดปฏิกิริยาและเสถียรภาพของซีเซียมเลดโบรไมด์ที่ห่อหุ้มด้วยไทเทเนียมไดออกไซด์สำหรับกระบวนการโฟโตคะตะลิติกด้วยตัวเร่งปฏิกิริยาของโรดามีน บี

น.ส.นัสซียา ปลายเนิน

วิทยานิพนธ์นี้เป็นส่วนหนึ่งของการศึกษาตามหลักสูตรปริญญาวิศวกรรมศาสตรมหาบัณฑิต
สาขาวิชาวิศวกรรมเคมี ภาควิชาวิศวกรรมเคมี
คณะวิศวกรรมศาสตร์ จุฬาลงกรณ์มหาวิทยาลัย
ปีการศึกษา 2566

Thesis Title	Activity and stability of TiO_2-encapsulated $CsPbBr_3/Cs_4PbBr_6$ for photocatalytic degradation of Rhodamine B
By	Miss Nutzeya Plainoen
Field of Study	Chemical Engineering
Thesis Advisor	Associate Professor Paravee Vas-Umnuay, Ph.D.
Thesis Co Advisor	Professor*Jeffrey Chi-sheng Wu, Ph.D.

Accepted by the FACULTY OF ENGINEERING, Chulalongkorn University in Partial Fulfillment of the Requirement for the Master of Engineering

.... Dean of the FACULTY OF ENGINEERING
(Professor SUPOT TEACHAVORASINSKUN, D.Eng.)

THESIS COMMITTEE

.... Chairman
(Associate Professor KASIDIT NOOTONG, Ph.D.)
.... Thesis Advisor
(Associate Professor Paravee Vas-Umnuay, Ph.D.)
.... Thesis Co-Advisor
(Professor*Jeffrey Chi-sheng Wu, Ph.D.)
.... Examiner
(Akawat Sirisuk, Ph.D.)
.... External Examiner
(Tanyakorn Muangnapoh, Ph.D.)

นัสซียา ปลายเนิน : การเกิดปฏิกิริยาและเสถียรภาพของซีเซียมเลดโบรไมด์ที่ห่อหุ้มด้วยไทเทเนียมไดออกไซด์สำหรับกระบวนการโฟโตคะตะลิติกด้วยตัวเร่งปฏิกิริยาของโรดามีน บี. (Activity and stability of TiO_2-encapsulated $CsPbBr_3/Cs_4PbBr_6$ for photocatalytic degradation of Rhodamine B) อ.ที่ปรึกษาหลัก : ปารวี วาศน์อำนวย, อ.ที่ปรึกษาร่วม : เจฟฟรี่ ฉี่-เชิง อู่

เนื่องจากซีเซียมลีดโบรไมด์เพอรอฟสไคต์ ($CsPbBr_3$) มีประสิทธิภาพในด้านออปโตอิเล็กทรอนิกส์ที่ยอดเยี่ยมแล้วยังเป็นตัวเลือกที่มีศักยภาพในการเป็นตัวเร่งปฏิกิริยาด้วยแสงสำหรับกระบวนการย่อยสลายสารประกอบอินทรีย์ภายใต้แสงอาทิตย์ โดยในระหว่างการสังเคราะห์ซีเซียมลีดโบรไมด์($CsPbBr_3$) จะพบการเกิดซีเซียมลีดโบรไมด์อีกรูปแบบที่มีสูตรโมเลกุลดังนี้ Cs_4PbBr_6 ซึ่งมีคุณสมบัติเด่น เช่น โฟโตลูมิเนสเซนซ์(PL) หรือคุณสมบัติการเรืองแสงของสารกึ่งตัวนำที่ดีมากอีกทั้งยังสามารถเพิ่มความเสถียรต่อการทนความร้อนที่สูงขึ้น โดยในงานวิจัยฉบับนี้ทางคณะผู้วิจัยสามารถสังเคราะห์อนุภาคนาโนที่มีรูปแบบผสมระหว่าง $CsPbBr_3$ และ Cs_4PbBr_6 ด้วยวิธีการตกตะกอนอย่างง่ายได้สำเร็จ ทว่าความเสถียรของตัวเร่งปฏิกริยาชนิด $CsPbBr_3/Cs_4PbBr_6$ มีความไวต่อสภาวะที่มีอุณหภูมิ ความชื้น และออกซิเจนที่สูง ซึ่งส่งผลต่อประสิทธิภาพในการย่อยสลายด้วยแสงได้โดยตรง ดังนั้นเพื่อเพิ่มความเสถียรและประสิทธิภาพของตัวเร่งปฏิกริยา ทางผู้วิจัยใช้เทคนิคการเปลี่ยนรูปด้วยน้ำแบบขั้นตอนเดียว(one-step water-triggered transformation) วิธีนี้เป็นนวัตกรรมที่ห่อหุ้มนาโนอนุภาค $CsPbBr_3/Cs_4PbBr_6$ ไม่ให้สัมผัสน้ำและเงื่อนไขที่ทำให้เสื่อมสภาพโดยตรงด้วยชั้นป้องกันที่ประกอบด้วยไทเทเนียมไดออกไซด์(TiO_2) โดยสามารถสรุปความสัมพันธ์ระหว่างสารทั้งสองชนิดให้อยู่ในรูปแบบของคอมโพสิท/โลหะ-ไดออกไซด์ ซึ่งคอมโพสิทเหล่านี้มีบทบาทสำคัญในกระบวนการถ่ายโอนและแยกประจุอย่างมีประสิทธิภาพ ซึ่งเป็นสิ่งสำคัญในกระบวนการโฟโตคะตาไลติก ในงานวิจัยฉบับนี้ผู้วิจัยศึกษาการปรับอุณหภูมิสังเคราะห์ (95, 110, 125, และ140 องศาเซลเซียส) เงื่อนไขการอบแห้ง(80 องศาเซลเซียสเป็นเวลา 2 ชั่วโมง, 80 องศาเซลเซียสเป็นเวลา 12 ชั่วโมงและที่อุณหภูมิห้องเป็นเวลา 12 ชั่วโมง) สุดท้ายที่การปรับอัตราส่วนโดยมวลระหว่าง $CsPbBr_3/Cs_4PbBr_6$ ต่อไทเทเนียมไดออกไซด์ (1:1, 1:2, 1:3, และ 1:4) ที่อาจส่งผลต่อการเพิ่มความเสถียรของตัวเร่งปฏิกริยาได้และผลลัพธ์แสดงให้เห็นว่าเราสามารถปรับปรุงความเสถียรและความสามารถในย่อยสลายทางแสงของตัวเร่งปฏิกริยาได้โดยการเลือกอุณหภูมิสำหรับการสังเคราะห์ที่ 95 องศาเซลเซียสและอุณหภูมิอบแห้งที่ 80 องศาเซลเซียสเป็นเวลา 2 ชั่วโมง โดยเมื่อเลือกอัตราส่วนโดยมวลระหว่าง $CsPbBr_3/Cs_4PbBr_6$ เป็น 1:3 จะพบว่าตัวเร่งปฏิกริยาจะมีพื้นที่ผิวจำเพาะสูงสุดที่ 222 ตารางเมตร/กรัม ซึ่งทำให้มีการดูดซึมระหว่างเข้าสมดุลและการย่อยสลายทางแสงของโรดามีน บี ที่ค่าสูงสุดด้วยค่าคงที่ของอัตราการย่อยสลาย(k) อยู่ที่ 0.1053 นาที$^{-1}$ และเกิดกระบวนการโฟโตคะตะลิติกได้อย่างสมบูรณ์ภายใน 30 นาที

สาขาวิชา วิศวกรรมเคมี ลายมือชื่อนิสิต ....
ปีการศึกษา 2566 ลายมือชื่อ อ.ที่ปรึกษาหลัก ....
ลายมือชื่อ อ.ที่ปรึกษาร่วม ....

6470385721 : MAJOR CHEMICAL ENGINEERING

KEYWORD: Photocatalyst, CsPbBr3, TiO2, Photocatalytic Degradation, Stability

Nutzeya Plainoen : Activity and stability of TiO_2-encapsulated $CsPbBr_3/Cs_4PbBr_6$ for photocatalytic degradation of Rhodamine B. Advisor: Assoc. Prof. Paravee Vas-Umnuay, Ph.D. Co-advisor: Prof.*Jeffrey Chi-sheng Wu, Ph.D.

Due to the excellent optoelectronic performance of cesium lead bromide($CsPbBr_3$), it has shown promising potential as a photocatalyst for the degradation of organic compounds under sunlight. During the synthesis of $CsPbBr_3$, Cs_4PbBr_6, another formation of $CsPbBr_3$, is also produced, which exhibits desirable properties such as strong and narrow photoluminescence (PL) and enhanced thermal stability. In this study, we successfully synthesized a mixture of $CsPbBr_3/Cs_4PbBr_6$ nanoparticles using a simple precipitation method. However, the stability of $CsPbBr_3/Cs_4PbBr_6$ was found to be sensitive to high temperatures, moisture, and oxygen, which could affect its photocatalytic degradation performance. To enhance both stability and activity, we employed the technique called the one-step water-triggered transformation method by encapsulating $CsPbBr_3/Cs_4PbBr_6$ nanoparticles with a protective layer of titanium dioxide (TiO_2), creating a perovskite/metal-oxide composite. This composite plays a crucial role in facilitating efficient charge transfer and separation, which are essential for successful photocatalytic processes. To achieve optimal results, we varied the reaction temperatures (95, 110, 125, and 140°C), drying conditions (80°C for 2 h, 80°C overnight, and at room temperature overnight), and mass ratio between $CsPbBr_3$/ Cs_4PbBr_6 to tetrabutyl titanate (1:1, 1:2, 1:3, and 1:4). The results demonstrated that the stability of TiO_2-encapsulated $CsPbBr_3$/ Cs_4PbBr_6 could be significantly enhanced by undergoing a reaction temperature of 95 °C and drying condition at 80 °C for 2 h. Moreover, when the mass ratio between $CsPbBr_3/Cs_4PbBr_6$ was set at 1:3, the material exhibited a maximum surface area of 222 m^2/g, resulting in the highest absorption and degradation activity. The kinetic rate constant was determined at 0.1053 min^{-1}, enabling complete photocatalytic degradation within 30 min.

Field of Study:	Chemical Engineering	Student's Signature ....
Academic Year:	2023	Advisor's Signature ....
		Co-advisor's Signature ....

ACKNOWLEDGEMENTS

This thesis presents the outcomes of a collaborative project conducted under the double degree program between Chulalongkorn University in Thailand and National Taiwan University in Taiwan. I would like to express my sincere gratitude to my two advisors, Associate Professor Paravee Vas-Umnuay and Professor Jeffrey Chi-Sheng Wu, from both countries, for their invaluable support and guidance throughout the research process, their mentorship has been instrumental in this study, and I am also grateful for the support and encouragement I received, which helped me overcome challenges along the way. Special thanks to all committees for providing clear research directions, enabling me to focus on the development of this research. Moreover, I am indebted to the members of the Catalysis and Reaction Engineering Laboratory in Taiwan, who have been assisting me since my first step into the lab. Their kindness, friendliness, and cooperation have been greatly appreciated. I would like to acknowledge the staff at National Taiwan University and Chulalongkorn University for their assistance in accessing and utilizing the necessary equipment for result analysis. Lastly, I want to express my heartfelt appreciation to my parents for their unwavering support and encouragement, which have been crucial in pursuing my dreams and successfully traversing this path and thankful for the overall atmosphere and everything that surrounded me, allowing me to complete this research endeavor.

Nutzeya Plainoen

TABLE OF CONTENTS

Page

LIST OF TABLES

LIST OF FIGURES

Page

Chapter 1

Introduction

1.1 Background

The textile dyeing industry is the second-largest industry that generates wastewater worldwide; with the continuous growth of the fashion industry, it has resulted in an increase of more than 20% in the generation rate of textile wastewater [1]. Chemical dyes that bond with the fabric is commonly used to provide and retain richer colors throughout washing and exposure. However, wastewater from textile contains a high concentration of organic and inorganic substances, such as salts, acids, alkalis, and heavy metals. Of particular concern are the dyes themselves, which consist of organic compounds with two groups. Within their molecules, dyes possess two essential components: the chromophore and the auxochrome. Chromophores commonly found in dyes comprise azo (-N=N-), nitro ($-NO_2$), nitroso (-N=O), thiocarbonyl (-C=S), and alkenes (-C=C-)[2]. These substances can pollute water sources and harm aquatic life, posing a threat to the environment and human health.

The degradation of dyes through photodegradation is regarded as a highly promising technology for treating industrial wastewater, specifically targeting the elimination of organic pollutants resulting from chemical dyes employed in textile dyeing processes. Photodegradation provides an eco-friendly and economical approach, ensuring that no secondary pollution is generated, making it a desirable solution[3]. Photocatalysis often utilizes semiconductor materials like TiO_2 or Wo_3, which have been traditionally employed. However, dyes possess the ability to absorb light radiation within the visible spectrum, encompassing wavelengths ranging from 380 to 750 nm[4]. However, these photocatalysts are only effective in the ultraviolet range according to the solar radiation spectrum; Whereas the visible light wavelength range accounts for more than 42.3% of the overall solar spectrum compared to the ultraviolet wavelength range (100-400 nm) which accounts for only 9% [5]. Hence, an inorganic perovskite with the structure of ABX_3 has become one of the good candidates that can absorb sunlight in the visible wavelength. The perovskite is composed of a monovalent cation (A), a divalent cation (B), and a halogen counterion (X) [6]. This material has a stable crystalline structure and a high photoluminescence quantum yield, making it efficient in converting absorbed light into emitted light. In addition, it is widely used in light-emitting diodes and water-splitting systems.

In this study, cesium-lead-perovskite $CsPbX_3$ (X = Cl, Br, and I) with Br^- as the anion was chosen due to its relative stability compared to other halogen compounds and its affordability for photocatalysis compared to other semiconductors such as $CsPbI_3$ [7]. Furthermore, $CsPbBr_3$ has an energy band gap (∼2.3 eV) that matches with the wavelength of sunlight in the visible spectrum, making it an ideal candidate for visible light photocatalysis. During the synthesis of $CsPbBr_3$, Cs_4PbBr_6, another formation of $CsPbBr_3$, is also produced, which exhibits desirable properties such as strong and narrow photoluminescence (PL) and enhanced thermal stability. However, perovskite materials are susceptible to degradation when exposed to moisture, oxygen, or elevated temperatures, which can lead to instability and reduced photocatalytic activity [7]. To address this issue, encapsulation of $CsPbBr_3/Cs_4PbBr_6$ nanoparticles by TiO_2 can be a solution to improve the stability of $CsPbBr_3/Cs_4PbBr_6$ by acting as a protective layer. Moreover, the properties of TiO_2 are high stability with wide bandgap, and strong absorption in the UV spectrum, resulting in higher absorption of light in both visible and UV wavelength ranges [8]. The encapsulation of $CsPbBr_3/Cs_4PbBr_6$ by TiO_2 can also help to prevent the migration of heavy metals into the environment, making it an environmentally friendly option for wastewater treatment.

1.2 Research objectives

To improve the stability of $CsPbBr_3/Cs_4PbBr_6$ in the photolysis by encapsulated TiO_2

1.2.1 To investigate the effect of synthesis temperature on $CsPbBr_3/Cs_4PbBr_6$ nanoparticle on photocatalytic activity of Rhodamine B degradation.

1.2.2 To investigate the effect of mass ratio between $CsPbBr_3/Cs_4PbBr_6$ and tetrabutyl titanate on stability of catalyst and its photocatalytic activity of Rhodamine B degradation.

1.3 Research scope

1.3.1 $CsPbBr_3/Cs_4PbBr_6$ nanoparticles were synthesized using a simple precipitation method. The reaction temperature was varied at 95, 110, 125, and 140 ℃

1.3.2 Encapsulation of $CsPbBr_3/Cs_4PbBr_6$ by TiO_2 was performed using a one-step water-triggered transformation with a fixed amount of water at 25 microliters. The mass ratio between $CsPbBr_3$ and TBOT was varied from 1:1, 1:2, 1:3, and 1:4. The catalyst was placed in an autoclave at a fixed temperature of 150℃ and room temperature for 4 h.

1.3.3 n-hexane was used as a solvent.

1.3.4 The photodegradation system utilized a Xenon lamp (300W) with the distance from the light source to the beaker fixed at 7cm and 11 cm for height with the stirring rate at 250 rpm. The obtained photocatalyst of 20 mg was used as the photocatalyst, which was dispersed in a Rhodamine B solution of 50 mL with a concentration of 10 mg/L. Samples were taken using a syringe filter of 0.22 mm every 15 min and analyzed using a UV-Vis spectrophotometer.

Chapter 2

Literature review

Degrade the dye contamination by photolysis is one of the advance oxidation processes which use the photocatalysis normally involves reactions that utilize light and a semiconductor, known as a photocatalyst and when a semiconducting material is exposed to light, it triggers the formation of an electron-hole pair. The photocatalyst acts as a substrate that absorbs light and catalyzes chemical reactions.

2.1 Advance Oxidation Process

Advance Oxidation Process (AOP) The Advance Oxidation Process (AOP) is a sustainable approach that effectively eliminates various pollutants, including persistent organic pollutants (POPs), endocrine-disrupting compounds (EDCs), pharmaceuticals and personal care products (PPCPs), industrial chemicals, volatile organic compounds (VOCs), dyes, and other organic substances, contributing to cleaner and safer environments. This is accomplished by generating extremely reactive oxygen species, such as hydroxyl radicals and potent oxidizing agents, using various means such as ozone, hydrogen peroxide, or ultraviolet radiation, to degrade both organic and inorganic substances present in wastewater. Despite their short lifespan, these species are regarded as a superior approach compared to conventional methods due to their ability to convert stable oxidation products, such as carbon dioxide, water, and biodegradable organics[9, 10].

2.1.1 Photocatalysis

Photocatalysis is an advanced oxidation process by using photocatalyst to have an oxidation/reduction or break down the compounds in the presence of sunlight which can be classified into two types based on the physical state of the semiconductor and the reactant. Homogeneous photocatalysis occurs when both semiconductor and reactant are in the same phase, whether it is a gas, solid, or liquid. In contrast, heterogeneous photocatalysis happens when both semiconductor and reactant are in different phases. The classification of photocatalytic reactions into these two types helps in understanding the behavior of the system and in designing efficient photocatalytic processes for different applications [9]. The semiconductor has different band gap (E_g) which can classify the materials into three types, metal or conductor with E_g < 0.1 eV, semiconductor with E_g < 1.5-3.0 eV and insulator with E_g > 5.0 eV.

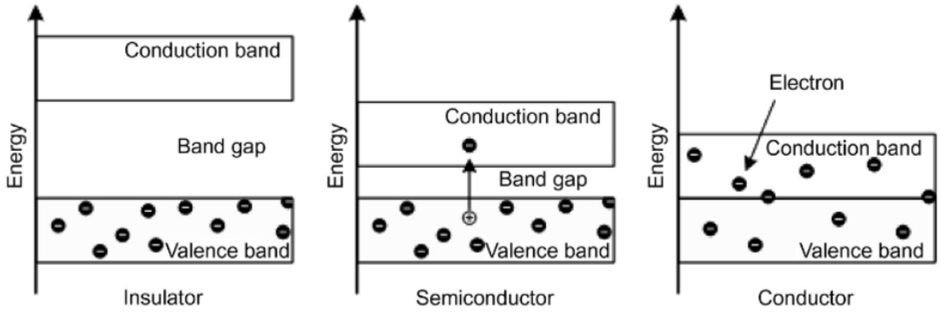

Figure 1 Different of materials [9]

The photocatalytic degradation of dyes using semiconducting materials, the process generally involves an indirect heterogeneous photocatalytic oxidation mechanism. This mechanism can be summarized as follows [11, 12].

1. Photoexcitation : Photoexcitation promoted from the filled valence band of a semiconductor photocatalyst, refers to the process in which an atom, molecule, or solid absorbs a photon of light and transitions from its ground state to an excited state. In photoexcitation, the absorbed photon provides energy to the system, causing one or more of its electrons to move to a higher energy level. The excited state may be short lived and result in emission of a photon (as in fluorescence), or it may lead to chemical reactions or other processes that involve the excited state. When a photon with energy ($h\nu$) equal to or greater than the band gap of the semiconductor photocatalyst is absorbed, the excitation process creates a hole in the valence band (h_{VB}^+). Consequently, this leads to the

generation of an electron-hole pair (e^-/h^+), as depicted by the equation (1) in which CB is conduction band and VB is valent band.

$$\text{Semiconductor} + h\nu\ (\text{UV light}) \longrightarrow \text{Semiconductor}\ (e_{CB}^- + h_{VB}^+) \qquad (1)$$

2. Ionization of water : Photogenerated holes in the valence band of a semiconductor can react with water to form hydroxyl radicals ($OH^\cdot$), which are highly reactive and powerful oxidizing agents, as expressed in equation (2). These radicals can then react with organic pollutants and break them down into smaller, less harmful compounds, or even mineralize them completely. Additionally, hydroxyl radicals can also attack microorganisms and thus provide enhanced decontamination.

$$H_2O + h_{VB}^+ \longrightarrow OH^\cdot + H^+ \qquad (2)$$

3. Photoinduced hole oxidation-reduction : The photogenerated hole (h_{VB}^+) can interact with certain molecules or species, such as water (H_2O) or hydroxide ions (OH^-), resulting in the generation of highly reactive hydroxyl radicals ($OH^\cdot$). At the same time, the photogenerated electrons (e_{CB}^-) in the conduction band of the semiconductor can participate in reduction reactions combine with suitable electron acceptors, such as molecular oxygen (O_2), leading to the production of anionic superoxide radicals (O_2^-), as shown in equation (3).

$$O_2 + e_{CB}^- \longrightarrow O_2^- \qquad (3)$$

The anionic superoxide radical (O_2^-) can also play a crucial role in preventing electron-hole recombination. This is because when the electrons in the conduction band (e_{CB}^-) of the photocatalyst combine with the holes in the valence band (h_{VB}^+), they effectively neutralize each other and reduce the overall efficiency of the photocatalytic process.

However, the presence of O_2^- can prevent this recombination by scavenging the photogenerated holes (h_{VB}^+) and effectively maintaining electron neutrality within the photocatalyst, thereby enhancing the overall efficiency of the process.

4. Protonation of superoxide : The superoxide ($O_2^{-\cdot}$) can undergo protonation to form the hydroperoxyl radical ($HO_2^\cdot$). The hydroperoxyl radical can then undergo further reactions to form hydrogen peroxide (H_2O_2), which can dissociate into highly reactive hydroxyl radicals ($OH^\cdot$), as shown in equations (4-8).

$$O_2^{-\cdot}\ H+ \rightleftarrows HO_2^\cdot \tag{4}$$

$$HO_2^\cdot \longrightarrow H_2O_2 + O_2 \tag{5}$$

$$H_2O_2 \longrightarrow 2OH^\cdot \tag{6}$$

$$\text{Dyes} + HO_2^\cdot \longrightarrow CO2 + H2O \tag{7}$$

$$\text{Dye} + h^+(VB) \longrightarrow \text{oxidation products} \tag{8}$$

$$\text{Dye} + e^-(CB) \longrightarrow \text{reduction products} \tag{9}$$

Semiconductors have the ability to facilitate light-induced redox processes by leveraging the electronic structure of their metal atoms in chemical compounds. This is primarily achieved through the presence of a filled valence band (VB) and an empty conduction band (CB), as depicted in Table 1.

Table 1 Bandgap energies (E_g) for common semiconductors [13].

Semiconductor	Bandgap energy (eV)	Semiconductor	Bandgap energy (eV)
Diamond	5.4	CdS	2.4
TiO_2	3.0-3.2	ZnS	3.7
WO_3	2.7	CdSe	1.7
ZnO	3.2	GaP	2.3
SnO_2	3.5	GaAs	1.4
$SrTiO_3$	3.4	SiC	3
Fe_2O_3	2.2		

TiO_2 and ZnO are commonly used as photocatalysts for photodegradation due to their wide bandgap, low cost, non-toxicity, stability under most environmental conditions, and eco-friendliness. However, these materials are only effective in the ultraviolet spectrum, with wavelengths ranging from 280 to 400 nm [14]. On the other hand, dyes have the ability to absorb light radiation in the visible spectrum, which ranges from 380 to 750 nm [4]. Therefore, the challenge is to choose and develop a more stable photocatalyst that can absorb a wider range of wavelengths, to achieve better photodegradation efficiency.

2.2 Sun spectrum

Solar radiation is a general term for the electromagnetic radiation emitted by the sun, which travels through space and reaches the Earth's atmosphere and surface. Infrared radiation makes up 49.4% of the total solar radiation, while visible light provides 42.3% and ultraviolet radiation accounts for just over 8%. Various technologies can harness solar radiation and convert it into useful forms of energy, including heat and electricity that can be divided into two categories. The first category is short-wave radiation, which comprises approximately 96% of the complete extra-terrestrial radiation within the spectral range [15]. It is a form of electromagnetic radiation that includes visible light, which can be subdivided into the prismatic colors of visible light containing wavelengths between 400-780 nm, and ultraviolet radiation (UV), which is usually subdivided into UV-A within the range of 315-400 nm, UV-B within the range of 280-315 nm, and UV-C within the range of 100-280 nm. The second category is long-wave radiation, which includes infrared (IR) radiation. It can be further divided into near infrared (NIR) containing wavelengths from 780 nm to 3**µ**m, and far infrared (FIR) containing wavelengths from 3**µ**m to 50 **µ**m. [15].

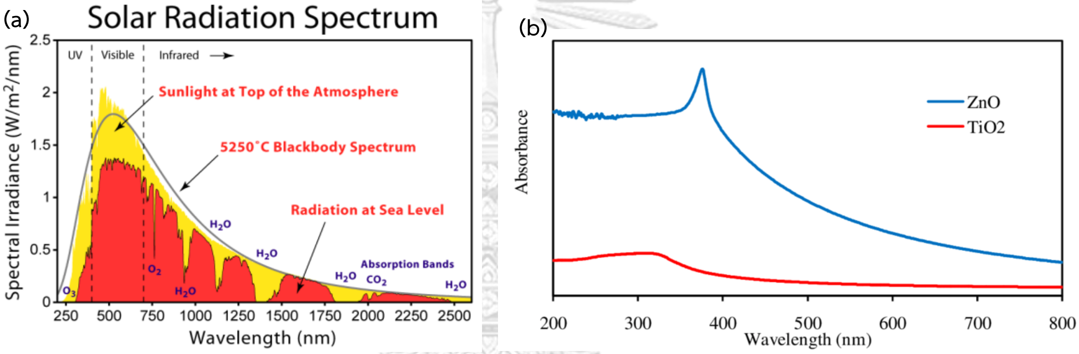

Figure 2 (a)The spectrum of solar radiation, (b)Absorbance of TiO_2 and ZnO nanoparticles in water [16]

2.3 $CsPbBr_3$

Inorganic perovskites have emerged as a potential solution to the chemical stability issues presented by organic/inorganic perovskites. The crystal structure of inorganic perovskites is not affected by temperature, which is vital for devices that will be exposed to solar radiation as it does not degrade their components [17, 18]. The photoactive layer of perovskite materials comprises chemical structures denoted as ABX_3, where A corresponds to a monovalent cation, such as Cs^+, positioned at the crystal's core. B is a divalent cation located in the corners, commonly Pb^{2+} has also been used, while X corresponds to an anion (usually a halogen counterion such as I^-, Br^-, or Cl^-) situated at the edges of the cubic cell's center. Ideally, perovskites have a cubic crystalline structure centered on the faces, which is the most desirable for their photovoltaic applications. Cesium-lead-perovskite $CsPbX_3$ (X = Cl, Br, and I) with Br- as the anion was chosen due to optical properties, such as tunable wavelength, narrow band, high quantum efficiency and its affordability for photocatalysis. Various studies have reported that $CsPbBr_3$ undergoes structural phase transitions from orthorhombic to tetragonal when the temperature exceeds 80℃, followed by a transition to cubic at temperatures above 130℃ [19-21]. Inorganic perovskites have a stable crystalline structure and a high photoluminescence quantum yield, making them efficient at converting absorbed light into emitted light. They are also widely used in light-emitting diodes and water-splitting systems.

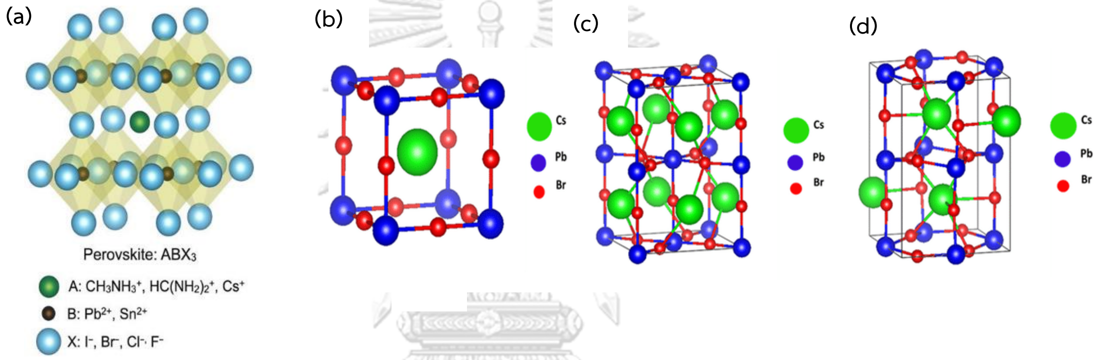

Figure 3 (a) Structure of ABX_3, Structure diagrams for the (b) cubic, (c) tetragonal and (d) orthorhombic phases of $CsPbBr_3$ [22]

Nonetheless, perovskites are prone to degradation when exposed to moisture, oxygen, or elevated temperatures, resulting in the fluorescence quenching which involve the formation of defects such as Pb-Br vacancies, which can act as nucleation sites for the formation of hydration shells around the $CsPbBr_3$'s surface. These hydration shells can ultimately lead to the dissolution, degradation of the material and reduced photocatalytic activity [23].

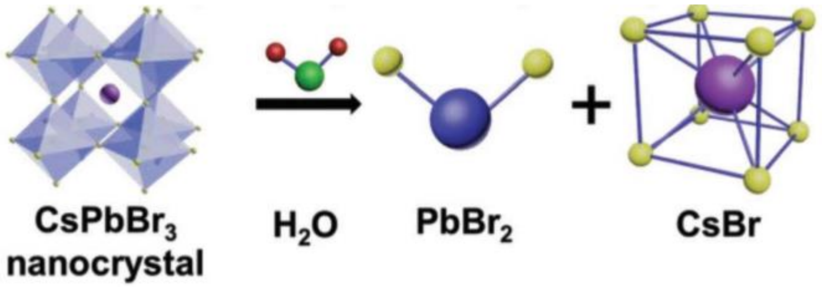

Figure 4 Fluorescence quenching of $CsPbBr_3$ nanocrystals [23]

2.3.1 $CsPbBr_3$ /Cs_4PbBr_6 composition

$CsPbBr_3$ perovskites are still being studied in the research community; however, it has been reported that the $CsPbBr_3$/Cs_4PbBr_6 composite exhibits enhanced quantum yield and stability due to surface passivation, interfacial emissive states, and spatial confinement of the $CsPbBr_3$ [24]. Specifically, the Cs_4PbBr_6 exhibits highly encouraging optoelectronic properties and displays promising characteristics such as strong and narrow photoluminescence (PL) which the emission wavelength and intensity of the photoluminescence can vary depending on the specific conditions and composition of Cs_4PbBr_6. Zhai et al. and Akkerman et al. reported that defect states within the large band gap of Cs_4PbBr_6 (Eg > 3.6 eV) result in green light emission to the embedded $CsPbBr_3$ in Cs_4PbBr_6 matrix [25-27]. The cubic $CsPbBr_3$ exhibits strong blue emission at a wavelength of 462 nm and attenuate a green emission at a wavelength of 529 nm with excellent optical properties . In contrast, Cs_4PbBr_6 has higher moisture stability and crystallizes in the rhombohedral phase. Zhong et al. reported that the green emission comes from Cs_4PbBr_6 crystals itself, but Cs_4PbBr_6 can be easily transformed into $CsPbBr_3$ via a CsBr-stripping mechanism or insertion reaction with additional $PbBr_2$ [28]. Palazon et al. reported that the transformation of $CsPbBr_3$ to Cs_4PbBr_6 is caused by the reinsertion of CsBr into $CsPbBr_3$ to form Cs_4PbBr_6 or the further extraction of $PbBr_2$ from $CsPbBr_3$ as described in the equation below [28].

$$Cs_4PbBr_6 + 3PbBr_2 \longrightarrow 4CsPbBr_3 \tag{10}$$

2.4 $CsPbBr_3$ /Cs_4PbBr_6 Synthesis

There are various methods available for synthesizing $CsPbBr_3$ /Cs_4PbBr_6, including sol-gel[29], simple precipitation [30], hot injection [31], typical antisolvent [32], wet-impregnation [33], anti-solvent precipitation [34], LARP technique [35] and emulsion methods [36]. Among the commonly used methods, the hot injection method and the antisolvent precipitation method are widely used. The hot injection method involves injecting a precursor solution containing Pb and Br ions into a hot solvent containing Cs ions, leading to the rapid nucleation and growth of $CsPbBr_3$ nanocrystals [31]. The antisolvent precipitation method involves adding an antisolvent to a precursor solution to induce the formation of $CsPbBr_3$ nanocrystals through rapid precipitation. Both methods offer good control over the size, shape, and properties of the resulting $CsPbBr_3/Cs_4PbBr_6$ nanocrystals. Although the antisolvent precipitation method may result in higher quality $CsPbBr_3$ nanoparticles, it also requires more precise control over the reaction conditions and may be more complex to carry out compared to simple precipitation which is relatively easy to perform, requires only simple laboratory equipment, and is suitable for the preparation of $CsPbBr_3$ nanoparticles with a narrow size distribution.

2.4.1 Simple precipitation method

The simple precipitation method, the precursors are mixed in a polar solvent, and a precipitating agent is added to the solution to form $CsPbBr_3$. The precipitating agent induces the reaction between the precursors, and the resulting $CsPbBr_3$ precipitates out of the solution. According to Yu, H et al. [37], adjusting the reaction temperature not only affects the morphology of $CsPbBr_3/Cs_4PbBr_6$ quantum dots but also influences their photoluminescence quantum yields (PL QYs). The absolute PL value decreases as the reaction temperature decreases, but if the temperature is increased above 160°C, the PL spectra will redshift from λmax = 517 nm to λmax = 521 nm, and the absolute PL QYs will decrease. Additionally, the crystal structure is dependent on the growth temperature. Higher temperatures (≥130°C) generally lead to a cubic phase, the X-ray diffraction (XRD) patterns presented in Figure 4 reveal that lower temperatures (<130°C) lead to the formation of an orthorhombic phase in $CsPbBr_3$. Specifically, at a temperature of 120°C, the XRD results indicate the presence of orthorhombic phase $CsPbBr_3$, as confirmed by the standard reference JCPDS, 00-054-0750. Conversely, temperatures higher than 130°C promote the formation of cubic $CsPbBr_3$, as evidenced by the XRD patterns and the standard reference JCPDS, 01-075-0412.

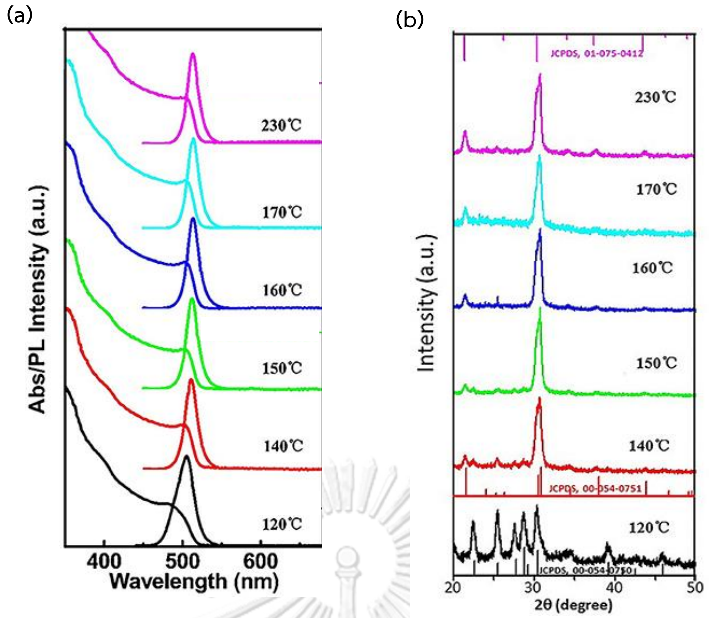

Figure 5 The pattern of $CsPbBr_3$ at different injection temperatures (a) UV-visible absorption and PL spectra, (b) The XRD pattern [37].

Bergamini et al. [30] investigated the use of $CsPbBr_3$ as a photo-electrode material in a photo-electrochemical cell, employing a novel approach of direct contact with water. The researchers employed a straightforward precipitation method to synthesize $CsPbBr_3$ and conducted a comprehensive characterization of its phase, morphology, and photocatalytic properties. The study further investigated the degradation rate of Rhodamine B under visible light exposure in two distinct reaction environments of water and ethyl acetate. The results confirmed that $CsPbBr_3$ particles exhibited photocatalytic activity in both water and ethyl acetate, with the highest degradation rate observed in the latter. After a duration of 60 min, the $CsPbBr_3$ catalyst successfully degraded 50% of the Rhodamine B.

2.5 Increasing the stability of $CsPbBr_3$ /Cs_4PbBr_6

Due to the instability of $CsPbBr_3/Cs_4PbBr_6$ when exposed to moisture, oxygen, or high temperatures, its photocatalytic activity can be reduced. To address this issue, several methods have been proposed to enhance the stability of $CsPbBr_3/Cs_4PbBr_6$, such as using composite materials with mesoporous silica nanoparticles and red photoluminescent quantum dots (PQDs) [38], doping with metals like nickel [39], applying a core shell of SiO_2 [40], or encapsulating it with Al_2O_3 [41], SiO_2 [42], or a polymer matrix [43]. However, for photocatalytic applications, it is important to consider both good stability, charge transport properties and resulting in higher absorption of light in both visible and UV wavelength ranges. Thus, among these methods, encapsulated by TiO_2 is a suitable candidate [44].

2.5.1 Encapsulate

Encapsulation refers to a process of coating solid particles, liquid droplets, or gas cells with a thin continuous layer of material, forming a capsule or shell around them. The purpose of encapsulation is to protect the inner content from external factors such as moisture, oxygen, and temperature, which can lead to degradation and reduced performance. In a recent study by Wenjing et al. [44], a one-step water-triggered transformation process was used to form $CsPbBr_3/Cs_4PbBr_6@TiO_2$ composites. From Figure 6, the study investigated the solvothermal reaction temperature at three different temperatures: 120, 150, and 180 ℃, with a fixed ratio of Cs_4PbBr_6 : TiO_2 at 1:3, and varying amounts of TBOT and water (25, 100, and 200 µl). The results showed that the solvothermal reaction temperature at 150℃ was the most suitable parameter. After encapsulation, the XRD analysis showed the absence of the TiO_2 diffraction peak, indicating that the TiO_2 was in an amorphous state (anatase) and excessive water addition to the reaction solution caused rapid hydrolysis of TBOT, leading to incomplete coating of the perovskite with TiO_2. This can have a negative impact on the sample's properties and performance, particularly in terms of its photocatalytic applications [44].

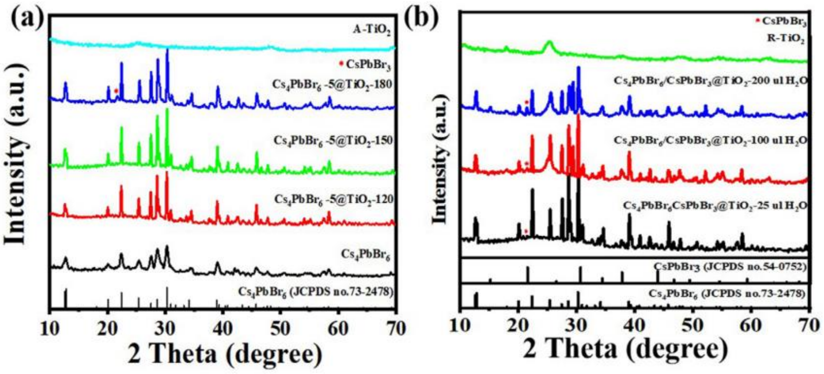

Figure 6 XRD patterns of $CsPbBr_3/Cs_4PbBr_6@TiO_2$ composites synthesized at (a) different reaction temperatures containing 25 mL H_2O in reaction solution, and (b) different amounts of water in encapsulation process at 150°C (the mass ratio of Cs_4PbBr_6 to TBOT is 1:3) [44].

2.6 Heterojunctions

There is probable that the interaction between $CsPbBr_3/Cs_4PbBr_6$ and TiO_2 involves the utilization of another semiconductor with distinct conduction and valence bands to enhance stability and optical properties. This process is referred to as forming three common types of heterojunctions based on band gap alignment from figure 7, and the details are as follows[45]

2.6.1 Straddling Gap Heterojunction (Type I)

Type I heterojunctions, an intricate alignment unfolds where the energy bands of one semiconductor material intricately coincide with those of its counterpart, establishing a harmonious "straddling" configuration. This elegant arrangement positions the conduction and valence bands of one material above the other, creating a discernible potential energy barrier for charge carriers at the interface. This nuanced heterojunction paradigm, characterized by its refined overlap, assumes significance in advanced technological applications, notably featuring in the development of sophisticated devices such as light-emitting diodes (LEDs) and laser diodes.

2.6.2 Straggred Gap Heterojunction (Type II)

Type II heterojunctions, a distinctive harmony emerges as the energy bands of one semiconductor material stagger relative to those of its counterpart. This staggered gap configuration introduces a notable discontinuity in both the conduction and valence bands at their interface. This specific alignment is often harnessed in sophisticated applications, such as solar cells and photodetectors, where the staggered band arrangement facilitates the effective separation of photo-generated electron-hole pairs. This nuanced heterojunction archetype, characterized by its band offset, plays a pivotal role in optimizing the performance of electronic devices with precision and efficiency.

2.6.3 Broken Gap Heterojunction (Type III)

The broken gap heterojunction refers to a situation where the conduction and valence bands of the two semiconductor materials do not align continuously at the interface. Instead, there is a discontinuity or misalignment in the band structure. This can lead to unique electronic properties and can be relevant in certain semiconductor devices

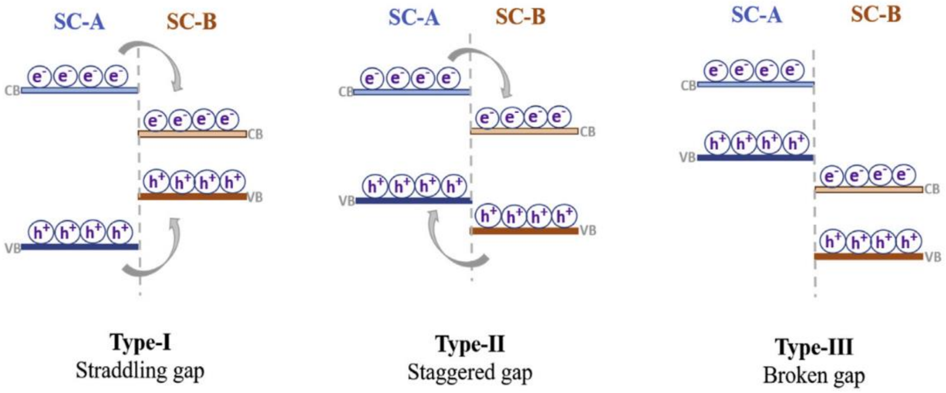

Figure 7 Different types of band alignment in Heterojunction[45]

2.7 Kinetic data

The degradation of Rhodamine B with $CsPbBr_3/Cs_4PbBr_6$ encapsulated by TiO_2 under the xenon lamp (300W) and samples were taken every 15 min using a syringe filter with a pore size of 0.22 μm and analyzed using UV-Vis spectrophotometer for 75 min. The photodegradation efficiency can be described by equation (11) [46].

$$\text{Degradation percentage/efficiency } (\boldsymbol{\eta}) = \frac{C_0 - C_t}{C_0} \times 100\ (\%) \qquad (11)$$

where, C_0 is the initial concentration (ppm) or absorbance at $\lambda_{max}$of dye, and

C_t is the concentration or absorbance (ppm) at λ_{max} of dye at time 't'

Ideally, the rate of a chemical reaction, or the rate constant (k_{obs}), can be described by a first-order rate expression. This means that the reaction rate is directly proportional to the concentration (or pressure) of the reactant molecules. The proportion of molecules with enough kinetic energy to overcome the activation energy barrier is determined by the temperature of the reaction. Higher temperatures result in higher average kinetic energy and a greater proportion of molecules with sufficient energy for the reaction to occur. Additionally, the actual number of molecules possessing this energy is influenced by the concentration (or pressure) of the reactants. Higher reactant concentrations lead to a higher rate of successful collisions and, consequently, an increased reaction rate. Understanding the relationship between temperature, concentration, and the rate constant is crucial in predicting and controlling the rate of chemical reactions [47].

$$\ln\left(\frac{C_t}{C_0}\right) = -k_{obs}t \qquad (12)$$

For these reactions, pseudo first-order kinetics were employed by plotting the logarithm of substrate or product concentration against reaction time. This method yielded a linear equation (equation 11), which allowed for reconfirmation of the key parameters of the fitted curve between k_{obs} and SA/V. SA/V, which is the product of mass concentration (g/L) and specific surface area (m^2/g), is used as a general independent variable to correlate with the contaminant s' removal rate constants. This approach resulted in the attainment of a linear fitted curve with an R^2 value of 1 [48].

Chapter 3

Methodology

3.1 Preparation of $CsPbBr_3$ nanoparticles

3.1.1 List of chemicals

3.1.1.1 Cs_2CO_3 (cesium carbonate, 99.99%, thermos scientific)

3.1.1.2 $PbBr_2$ (Lead (II) bromide, 99.998% Thermo Scientific Chemicals)

3.1.1.3 1-octadecene (ODE, ≥90% Sigma-Aldrich, Germany)

3.1.1.4 Oleylamine (OLA, technical grade 70% Sigma-Aldrich, Germany)

3.1.1.5 Oleic acid (OA, technical grade 90% Sigma-Aldrich, Germany)

3.1.1.6 n-hexane (Honeywell, Germany)

3.1.2 Synthesis method

$CsPbBr_3/Cs_4PbBr_6$ nanoparticles were synthesized using a simple precipitation method proposed by Bergamini et al. [30]. To prepare the solution, 100 ml of 1-octadecene was loaded into a beaker with a stirring rate of 250 rpm. The temperature was raised to a fixed value (ranging from 95, 110, 125 to 140 ℃). Then, 5 mL of oleylamine and 5 mL of oleic acid were added to the solution. Next, 1 mmol of Cs_2CO_3 and 3 mmol of $PbBr_2$ were added, and the stirring rate was increased to 500 rpm. The resulting suspension turned from white to yellow, indicating the formation of the perovskite phase. The reaction was allowed to proceed for another 20 min before the suspension was cooled down to room temperature over a period of 50 min. The resulting product was washed with acetone by centrifuging at 2000 rpm for 30 min, followed by re-suspension in hexane by centrifugation at the same speed and duration. The catalyst nanoparticles were then dried using a vacuum dryer at 80℃ for 2 h and stored in a glass vial.

3.2 Preparation of $CsPbBr_3$ nanoparticles encapsulate by TiO_2

3.2.1 List of chemicals

3.2.1.1 $CsPbBr_3/Cs_4PbBr_6$ nanoparticles

3.2.1.2 n-hexane (Honeywell, Germany)

3.2.1.3 TBOT (Titanium (IV) n-butoxide, 99+%, Alfa Aesar)

3.2.1.4 Deionized water

3.2.2 Synthesis method

Titanium (IV) n-butoxide (TBOT) was prepared using a one-step water-triggered transformation method proposed by W. Zhu et al [44]., with varying mass ratios of $CsPbBr_3$: TBOT of 1:1, 1:2, 1:3, and 1:4 in 5 ml of n-hexane under ultrasonic treatment for 3 min. The resulting solution was then added dropwise into 50 mg of as-prepared $CsPbBr_3/Cs_4PbBr_6$ in 10 ml of n-hexane in a round bottom flask with a stirring rate of 260 rpm for 2 h. Subsequently, a solution containing 5 mL of n-hexane and 25 mL of water was added dropwise to the reaction mixture and stirred overnight. The resulting solution was transferred to a 25 mL teflon-lined autoclave and subjected to solvothermal reaction at 150℃ for 4 h. The product was washed with n-hexane by centrifuging at 2000 rpm for 30 min, then dried at room temperature using a vacuum dryer overnight and stored in a glass vial.

3.3 Photocatalyst test

3.3.1 System setup

A Rhodamine B solution with a concentration of 10 mg/L was prepared by dissolving 50 mL of Rhodamine B in deionized water. The photocatalyst obtained from 20 mg of the synthesized $CsPbBr_3/Cs_4PbBr_6$ was dispersed in the Rhodamine B solution. The mixture was brought to equilibrium under cover by being pretreated with an ultrasonic cleaner (DC300) for 10 min and then stirred in the dark under covered system for 20 min at 250 rpm. The system was set up with a 300W xenon lamp with the AM 1.5G (Arc Lamps Power Supply, 69911) as a light source, placed at a fixed distance of 7 cm and 11 cm above the center of the stirrer. After the equilibrium condition was reached, the light was turned on and samples were taken every 15 min using a syringe filter with a pore size of 0.22 μm and analyzed using UV-Vis spectrophotometer.

3.4 Photocatalyst characterizations

3.4.1 UV-visible spectrophotometer (UV-Vis, Cary 300)

UV-visible spectrophotometer measures the interaction between light and a sample by measuring absorption or reflection in the ultraviolet-visible light region. When a sample absorbs light, it causes an electron to jump from a ground state to an excited state, resulting in the production of a spectrum [49]. In this study, samples were prepared in powder form and measured in the wavelength range of 400-800 nm with scanning rate 240 nm per min to investigate the decrease of the peak at 554 nm.

3.4.2 Photoluminescence (PL, HITACHI, F-7000)

Photoluminescence spectroscopy is a method that involves the stimulation of photons from any material through a photo-excitation process, causing the material to jump to a higher electronic state. As the material relaxes and returns to a lower energy level, it releases energy in the form of photons. The signal obtained from the photo-induced electron-hole recombination in the samples can be used to measure the photoluminescence intensity, with higher intensity indicating a higher recombination rate and potential for high photocatalytic activity [50], [51], [52]. In this study, 3.5 mg of samples were dissolved in 12 ml of deionized water and measured at the excitation wavelength of 370 nm.

3.4.3 X-ray diffraction (XRD, Rigaku-Ultima IV)

X-ray diffraction is a technique used for examining crystal structures and atomic spacing. The method relies on the constructive interference of monochromatic X-rays in a crystalline sample. The interaction between the X-rays and the sample produces a diffracted ray, which satisfies Bragg's Law ($n\lambda = 2d\sin\theta$) [53]. This law relates the wavelength of the electromagnetic radiation to the diffraction angle and the lattice spacing in a crystalline sample by scanning the sample through a range of 2θ angles, all possible diffraction directions of the lattice can be obtained due to the random orientation of the powdered material. The diffracted X-rays are then detected, processed, and counted. Identification of the mineral can be achieved by converting the diffraction peaks to d-spacings, which can be compared with standard reference patterns since each mineral has a unique pattern [53]. In this study, samples in powder form were put on the plate, operating with Cu- Kα radiation and set the value from computer by 2θ = 10°- 60° , scan step is 0.01° and the counting time 0.5 sec/step.

3.4.4 Scanning Electron Microscopy (SEM, Nova NanoSEM 230)

Scanning Electron Microscopy (SEM) is a type of microscope that uses electrons instead of light to produce images. An electron gun located at the top of the microscope produces a beam of electrons that is directed towards the sample through a series of electromagnetic fields and lenses that focus the beam [54]. When the beam hits the sample, electrons and X-rays are emitted from its surface and are collected by detectors. These X-rays, backscattered electrons, and secondary electrons are then transformed into a signal and sent to a screen, which displays the final image that is similar to a television screen [54]. Furthermore, the equipment is equipped with Energy Dispersive X-ray spectroscopy (EDS) that is used to analyze the elemental composition of the sample [54]. In this study, the samples were placed on carbon tape on a platinum holder, which were then placed in the vacuum for 15 min before being put into the SEM machine.

3.4.5 Transmission Electron Microscope (TEM, the JEOL JEM-1200EX II)

The transmission electron microscope operates by using a high-energy beam of electrons instead of light, since the wavelength of electrons is much smaller than that of light, and the beam of electrons from the electron gun is focused into a small, thin, coherent beam using the condenser lens. The electrons can be scattered or diffracted by the atoms in the sample, allowing for observation of features such as the crystal structure, dislocations, grain boundaries, and defects. The detected electrons are then captured by a fluorescent screen or a digital camera to create an image of the sample [55]. In this study, the samples were prepared by dispersing them in deionized water and subjecting them to sonication for 10 min. The prepared samples were then deposited onto a lacey carbon film on 200-mesh copper grids (LC200-Cu) before being placed into the TEM machine.

3.4.6 Fourier-transform infrared spectroscopy (FTIR, Perkin Elmer Spectrum 100)

Fourier-transform infrared spectroscopy is a method used in infrared spectroscopy where infrared radiation is passed through a sample, and some of the radiation is absorbed by the sample, while some of it is transmitted. The resulting spectrum represents the molecular absorption and transmission, creating a molecular fingerprint of the sample which specific to each molecular structure, enabling the identification and characterization of different compounds based on their unique infrared spectra[56]. In this study, KBr was necessary for preparation because it has a transmittance of 100% in the wave number range of 4000-400, meaning it does not exhibit absorption in this range [57]. The samples were prepared using a mass ratio of 150:1 between KBr and catalyst, which means 0.3 g of KBr was used and 0.002 g of CsPbBr3 was added, finely ground in a mortar, and then pressed into sheets in a vacuum before being put into the FTIR, Perkin Elmer Spectrum 100.

3.4.7 X-ray photoelectron spectroscopy (XPS, Themo Fisher Scientific, Theta Phobe, Al-Kα X-ray)

X-ray photoelectron spectroscopy is a surface chemical characterization method that provides information about the surface properties, elemental composition, and electronic state of the elements present in a material. The XPS spectrum is measured by exposing the sample to a beam of X-rays. When the X-rays strike the surface of the sample, they interact with the electrons in the atoms of the sample, causing some of the electrons to be ejected from the surface [58]. These ejected electrons are called photoelectrons. The number of electrons and their kinetic energy is instantaneously assessed, which is related to the binding energy of the electrons to the atoms in the sample [59]. By analyzing the binding energies of the photoelectrons, it is possible to determine the chemical composition of the material's surface. In this study, the samples were prepared in powder form and the surface was cleaned using Argon gas, then they were measured under the Al-Kα X-ray source (1486.6 eV).

3.4.8 Brunauer-Emmette-Teller (BET, Micromeritics, ASAP 2010)

BET is based on the measurement of gas adsorption onto the surface area of solid or porous materials, used to determine the specific surface area of a material by measuring the amount of gas adsorbed onto its surface as a function of the relative pressure of the gas and assumes that the gas adsorption follows the multilayer adsorption phenomenon and that the surface is homogeneous and non-porous [60]. By plotting the amount of gas adsorbed as a function of the relative pressure, a specific type of isotherm called the BET isotherm is obtained. From this isotherm, the specific surface area of the material can be determined using the BET equation [60]. In this study, the catalyst was dried and de-watered on the surface, then heated up to 150°C under vacuum. After that, it was cooled down to 77K (the temperature of liquid nitrogen), and nitrogen gas was introduced to observe the surface absorption relative to the pressure. The BET equation was used to obtain the results.

Chapter 4

Results and Discussion

In this study, the effects of temperature and different ratios of $CsPbBr_3/Cs_4PbBr_6$ to tetrabutyl titanate(TBOT) on the stability and photodegradation efficiency of rhodamine B were investigated. The temperature control was adjusted in two stages. In the first stage, the synthesis was carried out at reaction temperatures of 95, 110, 125, and 140°C. In the second stage, the post-synthetic drying was conducted under vacuum conditions at 80°C for 2 h, 80°C overnight, and at room temperature overnight. Additionally, the ratio of $CsPbBr_3/Cs_4PbBr_6$ to TBOT varied as follows 1:1, 1:2, 1:3, and 1:4. The experimental results and discussions will be presented in the following order. In this report we define pure $CsPbBr_3/Cs_4PbBr_6$ as CPB_reaction temperature_dryer condition and TiO_2-encapsulated $CsPbBr_3/Cs_4PbBr_6$ as CT(mass ratio between $CsPbBr_3/Cs_4PbBr_6$ to TBOT)_reaction temperature_dryer condition

4.1 The effect of temperature

In the chemical reaction process, 1-octadecene acts as a natural solvent and contributes to the creation of arrays of hydrophobic corrals on the surface. It is mixed with oleic acid(OA) and olelamine(OAm) as reagents. When the specified temperature is reached, Cs_2Co_3 and $PbBr_2$ powders are added, resulting in an instantaneous reaction. The solution undergoes a color change from a clear liquid to a dark yellow solution due to the formation of perovskite. The expected reaction is Cs_2Co_3 reacts with OA to form Cs-oleate, and simultaneously, $PbBr_2$ binds with OA and OAm which act as ligands [61, 62]. OAm, in particular, functions as a surfactant or precursor to surfactants. It acts as a solvent for the reaction mixture and also serves as a coordinating agent to stabilize the particle surface, without undergoing any change in its chemical composition.

4.1.1 The effect of reaction temperature

Upon conducting a physical observation after synthesis, from Figure 8, it is evident that the color of the particles undergoes a noticeable change in response to the synthesis temperature, which is clearly visible to the naked eye. At a low temperature of 95°C, the catalyst exhibits a light-yellow color, gradually intensifying to a dull orange shade at the synthetic temperature of 140°C. Furthermore, based on the findings presented in Table 2, it was observed that the weight of particles increased significantly with increasing temperature because elevated temperatures provide more energy for the diffusion of precursor species, facilitating nucleation and particle coalescence. However, excessive temperatures during catalyst synthesis can lead to particle agglomeration or sintering. When examining the diameter of the catalyst, it was found that the synthesis temperature had no effect on the particle size. The average diameter remained consistent at about 2.947 Å. These results indicate that the synthesis temperature influences the reaction kinetics, leading to a greater amount of substance being produced.

Figure 8 Depicts the color of pure $CsPbBr_3/Cs_4PbBr_6$ after synthesis, under drying conditions at 80°C for 2 h, at different synthesis temperatures: 95, 110, 125, and 140°C, respectively, from left to right.

Table 2 Effect of synthesis temperature on catalyst quantity and particle size

Reaction Temperature (°C)	The average weight of catalyst (g)	Diameter of catalyst (Å)
95	0.118	2.963
110	0.184	2.942
125	0.367	2.947
140	0.644	2.952

Additionally, the synthesis temperature also affects the color of the particles when dissolved in a hexane solution. Particles synthesized at 95 °C exhibit a pale green fluorescence, while higher temperatures result in a pale-yellow solution. However, there are no observable differences when these solutions are observed in the dark under ultraviolet light. When considering the relationship between radiation range and wavelength, it can be inferred that temperature adjustment influences the absorption range of light at different wavelengths. Analyzing the data from Figure 9 reveals insights into the absorption of light versus wavelength by examining the point at which the curve begins to decline. Despite verifying variations in the synthesis temperature, the change becomes more pronounced as the reaction temperature increases. This indicates a noticeable rightward shift in the absorption spectrum. Although there is only a slight difference in details. It also observed that at a synthesis temperature of 140°C , the absorbance or intensity has a higher value compared to lower temperatures. This may be attributed to a higher amount of catalyst in the synthesis, making the substance more concentrated and reliable. Therefore, under the same equipment conditions but with different quantities, an increase in intensity is evident, as depicted in Figure 9.

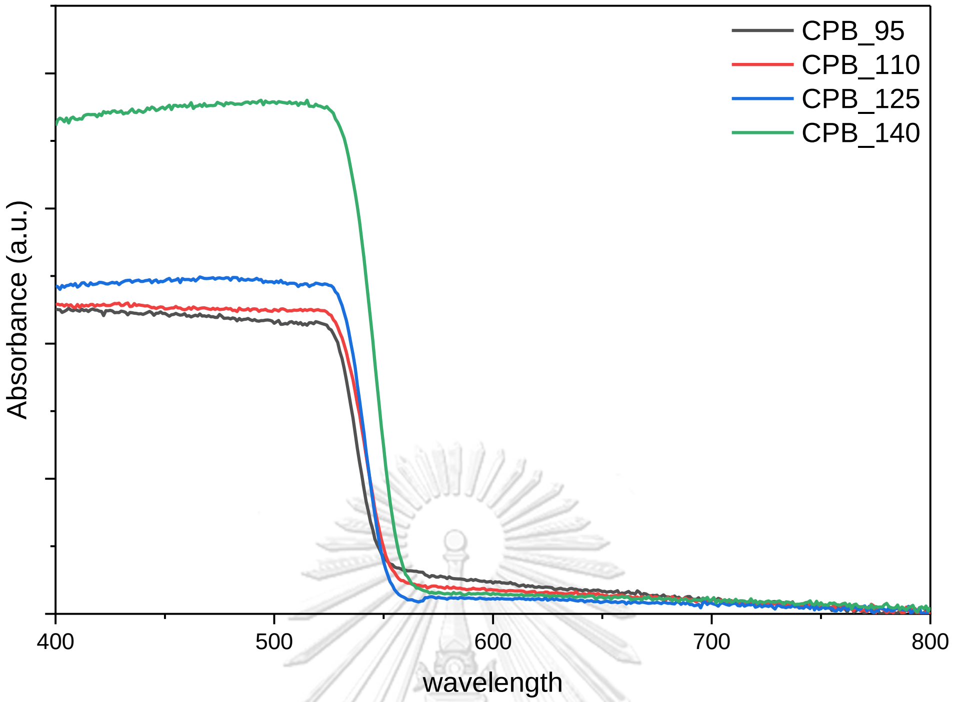

Figure 9 The absorbance of the UV-Vis spectrophotometer on the reaction temperature of the $CsPbBr_3/Cs_4PbBr_6$ under 80°C and 2 h of drying condition.

To check on crystal structure of catalyst in simple precipitation reactions, the influence of different synthesis temperatures on both morphology and formation of $CsPbBr_3$ and Cs_4PbBr_6 was observed, X-ray diffraction (XRD) analysis was conducted on each sample, as shown in Figure 10, revealing the transformation of Cs_4PbBr_6 nanocrystals (NCs) into $CsPbBr_3$ with increasing reaction temperature. At 95 °C, a noticeable peak was observed, primarily showing double peaks of Cs_4PbBr_6 at 12.59° (0 1 2), 12.82° (1 1 0), and 22.28° (3 0 0), while peaks of $CsPbBr_3$ were absent at 26.18° (1 1 1). The presence of multiple formations or mixed phases was observed, but the single peak around 30° in $CsPbBr_3$ or the cubic phase of $CsPbBr_3$ exhibited significantly different values. In the case of the orthorhombic phase, even peaks appeared with smaller and greater intensity at 30.66°, respectively. For other Cs_4PbBr_6 formations, peaks appeared at 30.12°.

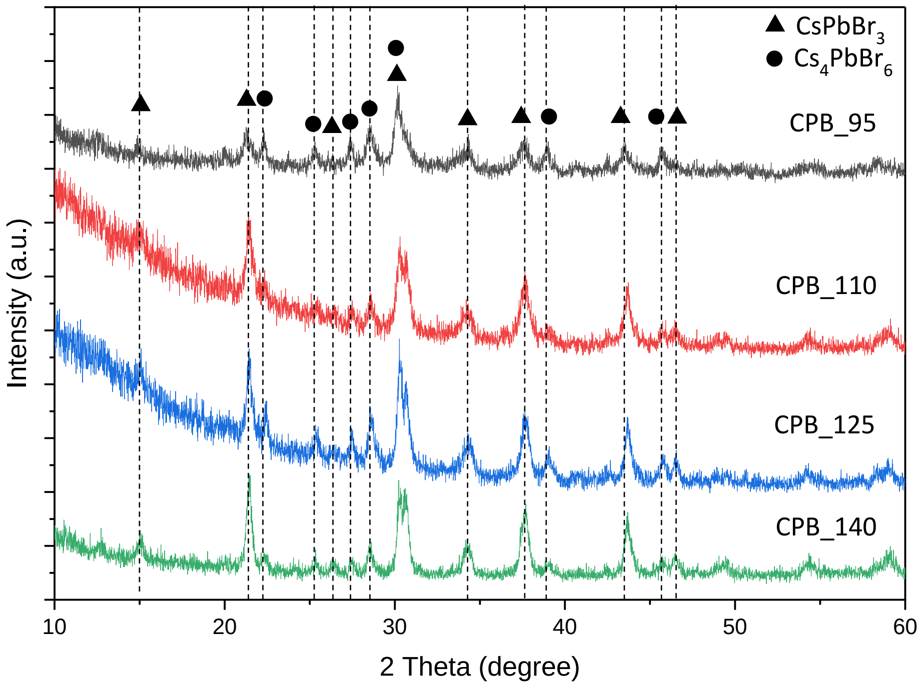

Figure 10 XRD patterns of $CsPbBr_3$ and Cs_4PbBr_6 composites synthesized at different reaction temperature under 80°C and 2 h of drying condition.

4.1.2 The effect of drying condition.

According to the referenced research, Cs_4PbBr_6 has demonstrated higher stability and improved photodegradation efficiency. Therefore, it is necessary to dry the catalyst in the final stage. In order to observe the changes in formation during drying, the catalyst was selected at a synthesis temperature of 95 °C and subjected to three different drying conditions at 80°C for 2 h, 80°C overnight, and at room temperature overnight. Figure 11a shows that when the catalyst was vacuum dried at room temperature, the formation of Cs_4PbBr_6 was preserved almost entirely without any significant influence from the drying temperature. This can be observed through the presence of the previously mentioned three peaks. However, when the drying temperature was raised to 80 °C, complete transformation of Cs_4PbBr_6 into $CsPbBr_3$ was observed. Additionally, when the drying time was reduced to 2 h, the observed peaks were less pronounced, indicating a mixed peak between $CsPbBr_3$ and Cs_4PbBr_6. This suggests that with a shorter drying time, the formation of $CsPbBr_3$ is incomplete, and the XRD pattern exhibits a mixed peak.

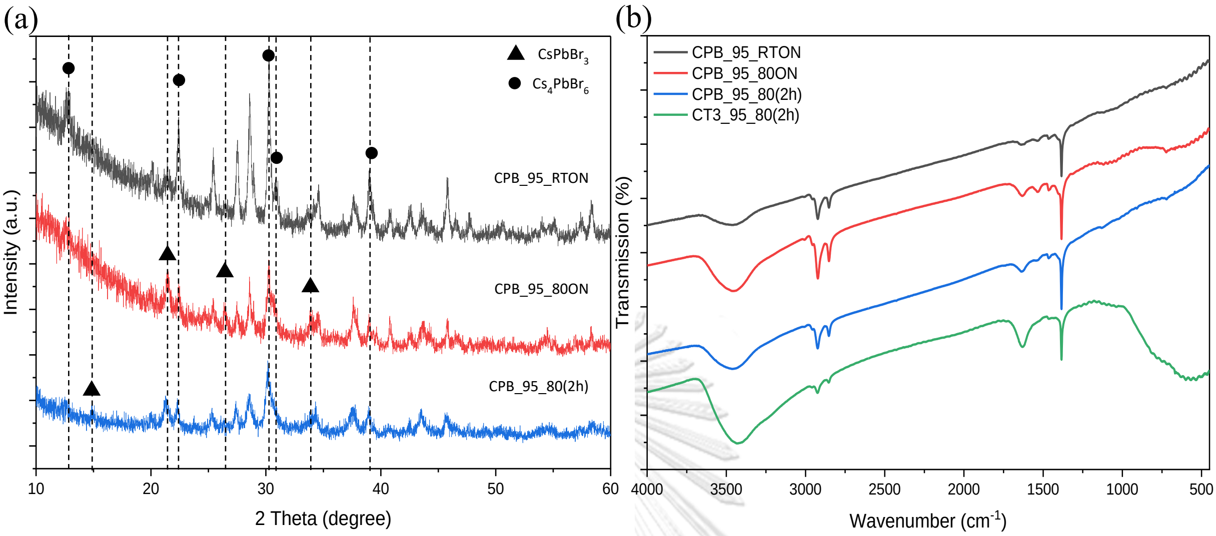

Figure 11(a) XRD patterns and (b) FT-IR pattern of $CsPbBr_3$ and Cs_4PbBr_6 formation composites synthesized under different drying conditions.

As observed in Figure 11b, the FT-IR results of $CsPbBr_3/Cs_4PbBr_6$, exhibit double peaks at 2923 cm^{-1} and 2853 cm^{-1}, which correspond to the $–CH_3$ group. The presence of these peaks suggests the remaining components from the reaction that may not have been completely washed off with n-hexane and acetone. Further analysis shows that after drying the catalyst overnight at 80 °C, the peak intensity of the $–CH_3$ group is significantly enhanced. However, the analyzed peaks at 1635 cm^{-1} and 3435 cm^{-1} demonstrate a distinct increase in intensity of the stretching vibration of hydroxyl groups (O-H) and surface absorbed water (H-O-H). This peak indicates the absorption of moisture or water molecules on the surface of the catalyst. The intensity of this peak provides insight into the amount of absorbed water and can be used to evaluate the moisture resistance. Notably, the peak at 3435 cm^{-1} indicates a higher concentration of water absorption, indicating a difference in drying conditions. Comparing among three cases, it is evident that overnight drying at room temperature had the least impact on the observed peaks. This suggests that it may not possess the same level of resistance to watery and humid conditions as the other two drying conditions.

4.2 The effect of ratio between $CsPbBr_3/Cs_4PbBr_6$ to TBOT

In order to address the issue of $CsPbBr_3/Cs_4PbBr_6$ losing its effectiveness under high humidity conditions, the incorporation of TiO_2 was explored as a potential solution. To achieve this, a one-step water-triggered transformation method was utilized under inter-process conditions at a constant temperature of 150 °C. During the investigation, TiO_2 was examined using the same synthesis process without $CsPbBr_3/Cs_4PbBr_6$, and a clear pattern of TiO_2 anatase at 2θ (25.33°) was observed, providing a reference point for further analysis.

For the synthesis of $CsPbBr_3/Cs_4PbBr_6$, a synthesis temperature of 95 °C was chosen, followed by drying at 80 °C for 2 h. The XRD analysis revealed a $CsPbBr_3/Cs_4PbBr_6$ peak around 25°, which closely resembled the 2θ value of anatase TiO_2. However, further investigation using XRD data indicated that the stabilization process at a constant temperature of 150 °C for 4 h did not significantly affect the formation of the compound. Therefore, it was confirmed that drying at 80 °C for 2 h was the optimal choice. During the drying step, the addition of water was necessary for hydrolysis, converting TBOT to TiO_2. The XRD pattern analysis in Figure 11a displayed a wide peak variation, suggesting structural changes. However, it was challenging to distinguish any significant differences in the 2θ value at 25.33° when varying the amount of water. On the other hand, when analyzing the samples using FT-IR in Figure 11b, interesting peaks are observed after encapsulation by TiO_2. A peak at 1384 cm^{-1} corresponds to the presence of aliphatic C-H functional groups (organic compounds), while a decrease in the peak intensity at 1468 cm^{-1} suggests the loss of COO- groups. Additionally, peaks at 1635 cm^{-1} and 3435 cm^{-1} indicate an increase in the intensity of hydroxyl groups (O-H) and surface-absorbed water (H-O-H).

Furthermore, the FTIR analysis reveals that the amount of water used in the hydrolysis process influences the bonding between Ti-O within the wavelength range of 618 cm^{-1}. Notably, the highest Ti-O content is observed with 5 μl of water, while there is no significant difference between the contents at 15 μl and 25 μl of water. This observation suggests that the higher Ti and O contents associated with 5 μl of water could be attributed to factors such as the surface area and bulk of the catalyst. However, further research is required to draw definitive conclusions in this regard.

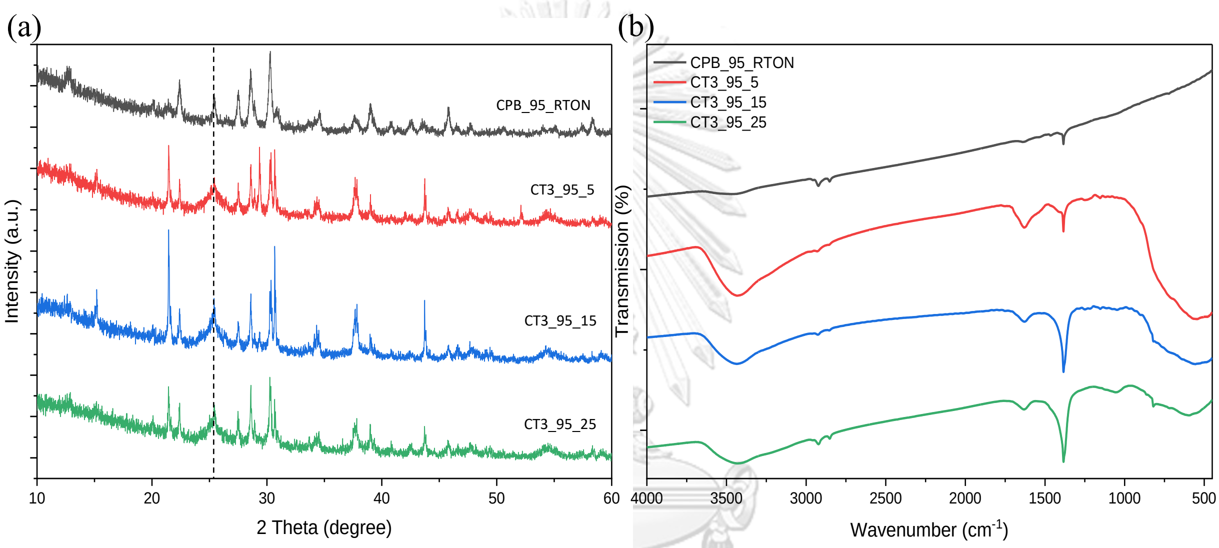

Figure 12 (a) XRD patterns and (b) FT-IR pattern of $CsPbBr_3$ and Cs_4PbBr_6 composites synthesized under different amounts of water in encapsulation process.

Therefore, based on previous studies and preliminary validations, a water content of 25 μl was selected to facilitate the hydrolysis process. Subsequently, the chosen amount of TBOT was used to investigate its effects on the stability and photodegradability of TBOT. From Figure 12, it can be observed that the TiO_2 peak is difficult to distinguish due to the overlapping peaks of $CsPbBr_3$/ Cs_4PbBr_6. Moreover, the synthesized TiO_2 in the process formed at 150 °C remains in an amorphous state and does not crystallize into TiO_2 anatase. However, increasing the ratio between $CsPbBr_3$/Cs_4PbBr_6 and TBOT leads to a wider peak around 2θ at 25.33°, indicating an influence of TBOT on the formation of TiO_2 on the catalyst. It is worth noting that there is no significant difference in peak width for ratios ranging from 1:2 to 1:4. Although it is challenging to ascertain the exact differences in TiO_2 produced during this variation process, visual inspection reveals the presence of white particles mixed with the yellow particles after synthesis, particularly with higher amounts of TBOT. This suggests that when the TBOT volume exceeds the $CsPbBr_3/Cs_4PbBr_6$ volume in the one-step water-triggered transformation method, the excess TBOT reacts with water to convert itself into TiO_2. Consequently, when the ratio between $CsPbBr_3/Cs_4PbBr_6$ and TBOT exceeds 1:4, the synthesized amount of TiO_2 in the final step significantly increases and surpasses the initial precursor amount of $CsPbBr_3/Cs_4PbBr_6$ used at the beginning of the process.

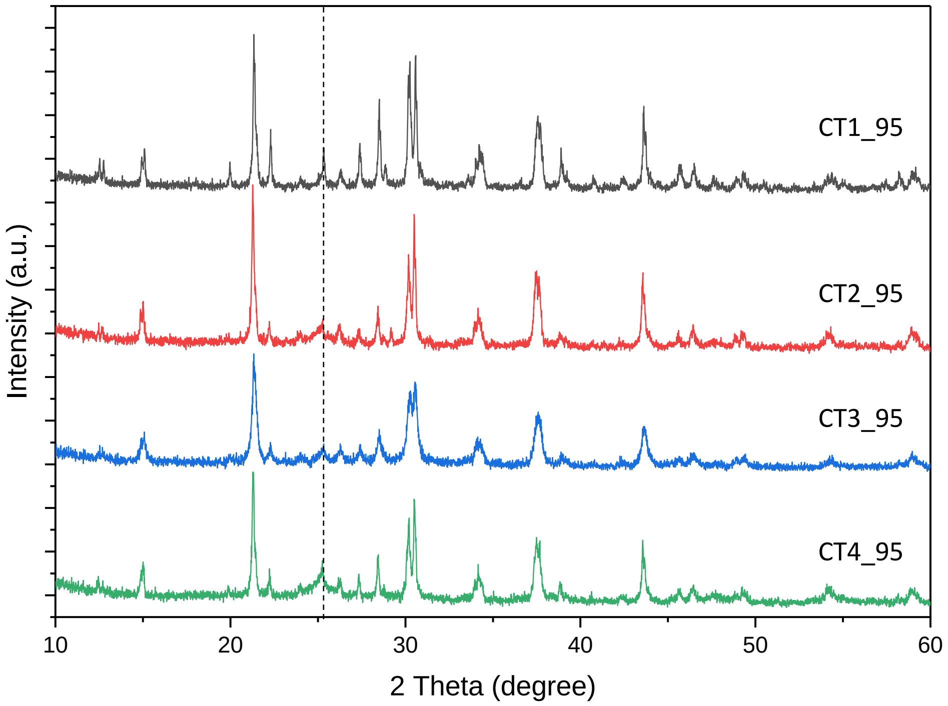

Figure 13 XRD patterns of $CsPbBr_3/Cs_4PbBr_6$ and $CsPbBr_3/Cs_4PbBr_6$ encapsulated by TiO_2 synthesized at different ratios of $CsPbBr_3/Cs_4PbBr_6$ to TBOT.

The influence of TBOT quantity on the BET surface area of the $CsPbBr_3/Cs_4PbBr_6$ catalyst can be observed from the data presented in Table 3. It is evident that the amount of TBOT has a significant impact on the resulting surface area. Specifically, when the $CsPbBr_3/Cs_4PbBr_6$ was synthesized with a TBOT ratio of 1:3, the catalyst exhibited the largest surface area. On the other hand, the 1:1 TBOT ratio resulted in the smallest surface area.

Table 3 BET surface area of TiO_2-encapsulated $CsPbBr_3/Cs_4PbBr_6$ by varying the mass ratio between $CsPbBr_3/Cs_4PbBr_6$ and TBOT under 80°C and 2 h of drying condition.

BET surface area (m^2/g)	
CT1_95	84.66
CT2_95	143.87
CT3_95	222.19
CT4_95	116.52

When examining the ratio of $CsPbBr_3/Cs_4PbBr_6$ to TiO_2 at 1:4, it was observed that the BET surface area did not increase with the TBOT content. This finding supports the previously mentioned idea that an excessive amount of TBOT can undergo self-hydrolysis, leading to the formation of a minor amount of TiO_2 compared to $CsPbBr_3/Cs_4PbBr_6$ encapsulated by TiO_2. Consequently, the detectable area becomes larger, indicating that the optimal point lies at a ratio of $CsPbBr_3/Cs_4PbBr_6$ to TiO_2 of 1:3. At this ratio, TiO_2 is present on top of $CsPbBr_3/Cs_4PbBr_6$ before the excess TBOT proceeds with hydrolysis. The size of the photocatalytic surface area can have a more direct impact on the stability and photodegradability of TBOT within the $CsPbBr_3/Cs_4PbBr_6$ catalyst system.

To validate the preliminary conclusion regarding the relative surface sizes of the compounds, further analysis was conducted using SEM, SEM mapping and EDS. The results, shown below, provide insights into the distribution of Ti, O, and other components on the catalyst. By examining the elemental composition and spatial arrangement.

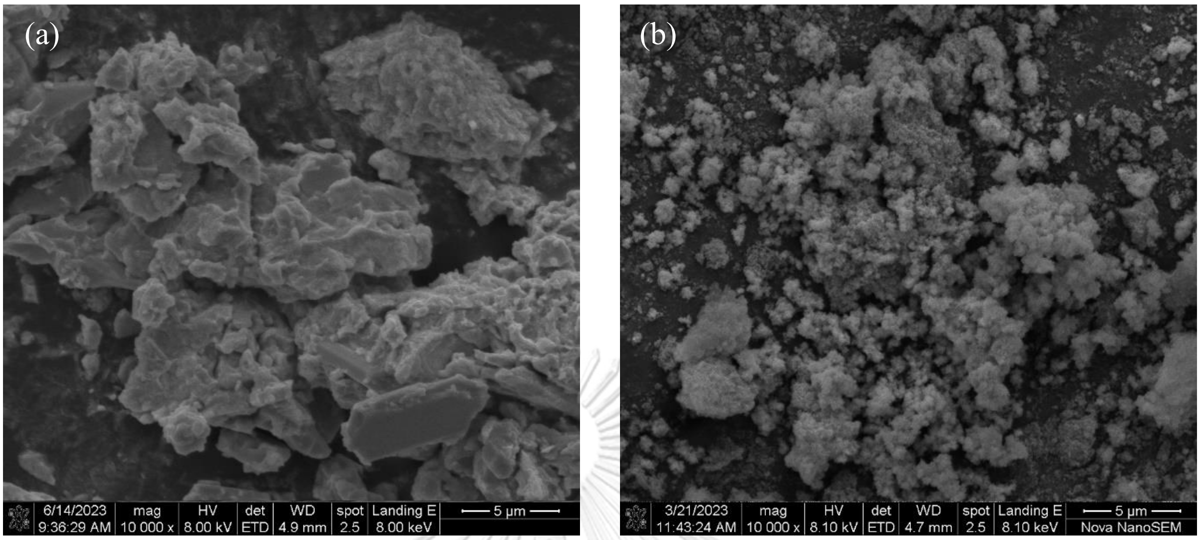

Figure 14 SEM images of (a) $CsPbBr_3/Cs_4PbBr_6$ and (b) $CsPbBr_3/Cs_4PbBr_6$ encapsulated by TiO_2 at 95°C prepared at the mass ratio between $CsPbBr_3/Cs_4PbBr_6$ to TBOT is 1:3.

Figure 14 shows the SEM results before and after the efficiency improvement. It can be observed that $CsPbBr_3/Cs_4PbBr_6$ aggregates with irregular shapes, poor crystallinity, or surface defects may have reduced photoactivity. However, after the renovation, although agglomeration still exists, the particles are noticeably more separated from each other. This improvement in morphology suggests an increase in photoactivity. Aggregates with a more homogenous shape and good crystallinity tend to exhibit better photoactivity due to enhanced charge transport and light absorption.

For further analysis, SEM mapping tests can be conducted to compare the case with the highest and smallest surface area by ratio between $CsPbBr_3/Cs_4PbBr_6$ to TBOT is 1:3 and 1:1 respectively, as depicted in the picture below.

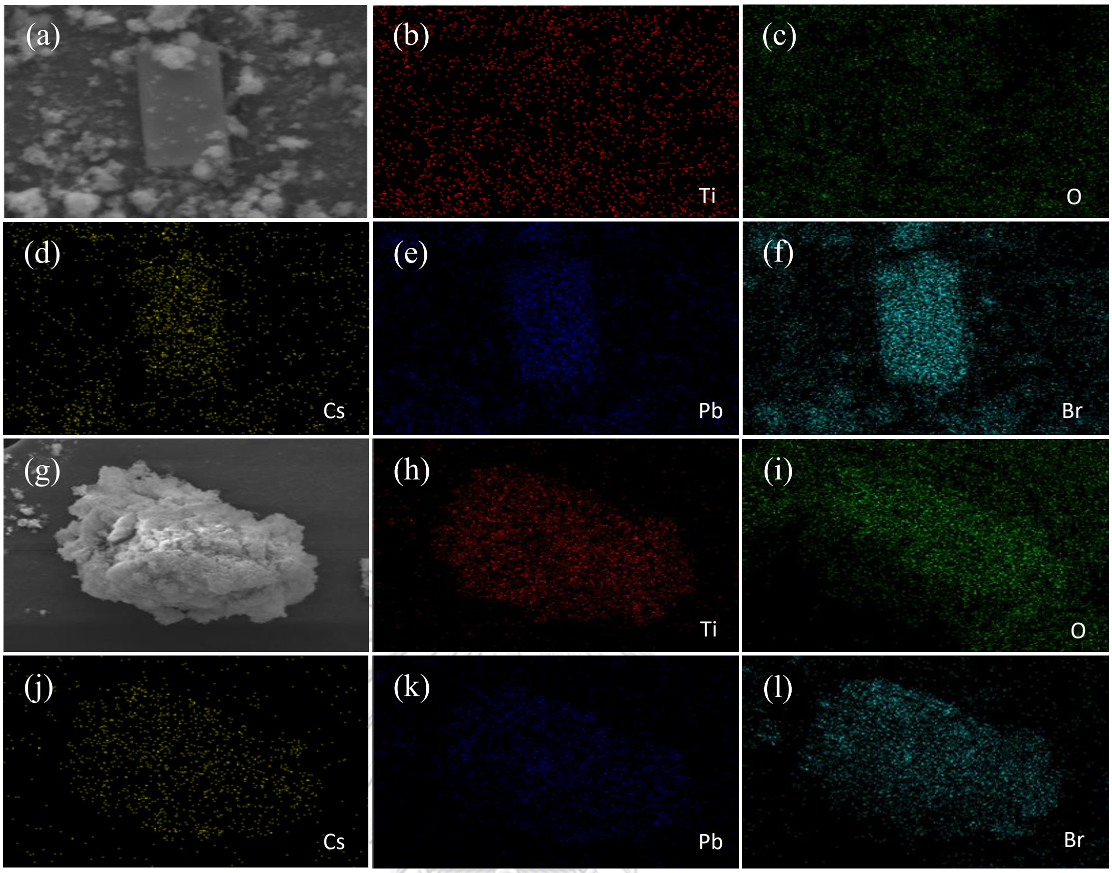

Figure 15 SEM elemental mapping images of $CsPbBr_3/Cs_4PbBr_6$ encapsulated by TiO_2 at 95°C prepared at the mass ratio between $CsPbBr_3/Cs_4PbBr_6$ to TBOT of (a-f) 1:1, and (g-l) 1:3.

From Figure 15b and 15c showing the SEM mapping, it was observed that in the $CsPbBr_3/Cs_4PbBr_6$ to TBOT ratios of 1:1 and 1:3, the Ti and O images did not appear clearly on the catalytic samples. This suggests that Ti may not adhere well to the surface of $CsPbBr_3/Cs_4PbBr_6$ or that the Ti content is too low to be easily detected. However, according to Table 4, the atomic ratio between Ti and O remains almost unchanged despite the varying ratios of $CsPbBr_3/Cs_4PbBr_6$ to TBOT. Based on these findings, it can be concluded that the ratio of $CsPbBr_3/Cs_4PbBr_6$ to TBOT at 1:1 result in a relatively low Ti content on the surface of $CsPbBr_3/Cs_4PbBr_6$. As the ratio increases to 1:3, the Ti content also increases, reaching an optimized value. For a ratio of 1:4, the atomic ratio remains nearly identical, indicating a similar abundance or proportion of elements. However, it is important to note that even if the atomic ratios are the same, it does not necessarily imply that the compounds are identical. Factors such as the arrangement of atoms, crystal structure, and bonding also play a role. Nonetheless, from Table 4, the observed catalyst exhibits a composition with a Cs:Pb:Br:Ti:O ratio of approximately 5.3:2.8:9.7:20.1:62.1. The excess TBOT leads to the formation of TiO_2 particles within the catalyst, although the amount of TiO_2 produced is too small to significantly impact photodegradation.

Table 4 Atomic ratio of $CsPbBr_3/Cs_4PbBr_6$ encapsulated by TiO_2 with by varying the mass ratio between $CsPbBr_3/Cs_4PbBr_6$ and TBOT under 80°C and 2 h. dry condition.

Catalyst	Cs	Pb	Br	Ti	O
CT1_95	9.8±8.1	3.7±2.3	10.9±3.5	17.2±4.0	58.5±9.9
CT2_95	8.0±4.5	5.8±4.2	19.0±14.6	18.0±11.4	49.1±14.7
CT3_95	5.3±2.5	2.8±1.1	9.7±3.4	20.1±0.8	62.1±7.8
CT4_95	4.5±1.6	2.6±0.8	9.0±2.7	19.5±1.2	64.3±6.2

Once the optimal ratio of $CsPbBr_3/Cs_4PbBr_6$ to TiO_2 at 1:3 was determined, we conducted XPS analysis on catalysts synthesized under different conditions. Specifically, we compared them to the CT3_95_80(2h) and CT3_95_80ON conditions to investigate whether formation of $CsPbBr_3/Cs_4PbBr_6$ and $CsPbBr_3$ in the synthesis process influenced the surface composition of the catalyst. We examined the relative abundance of Cs, Pb, Br, Ti, and O elements, and the results are depicted in Figure 16.

From Figure 16(a-d), CT3_95_80(2h), which corresponds to the formation of $CsPbBr_3/Cs_4PbBr_6$ with TiO_2, exhibits higher intensity compared to the case of CT3_95_80ON, which involves the formation of $CsPbBr_3$ with TiO_2. This higher intensity indicates a higher abundance or concentration of the corresponding elements on the sample surface. Additionally, in the high-resolution XPS spectra of Cs 3d, Pb 4f, and Br 3d regions, there is a higher relative abundance of Cs, Pb, and Br elements. Upon detailed analysis in Figure 14(b-d), a comparison with CPB_95_RTON, which represents pure $CsPbBr_3/Cs_4PbBr_6$. CT3_95_80ON reveals a leftward shift in the graph, while CT3_95_80(2h) exhibits a rightward shift. The shift to the right or negative shift in the XPS spectra observed in CT3_95_80(2h) suggests stronger bonding and electronic interactions between Cs_4PbBr_6 and the TiO_2 shell in the $CsPbBr_3/Cs_4PbBr_6$ and TiO_2 composite structure. This shift indicates a greater degree of charge transfer and coupling between the two components, implying a more intimate and efficient interaction at the atomic level.

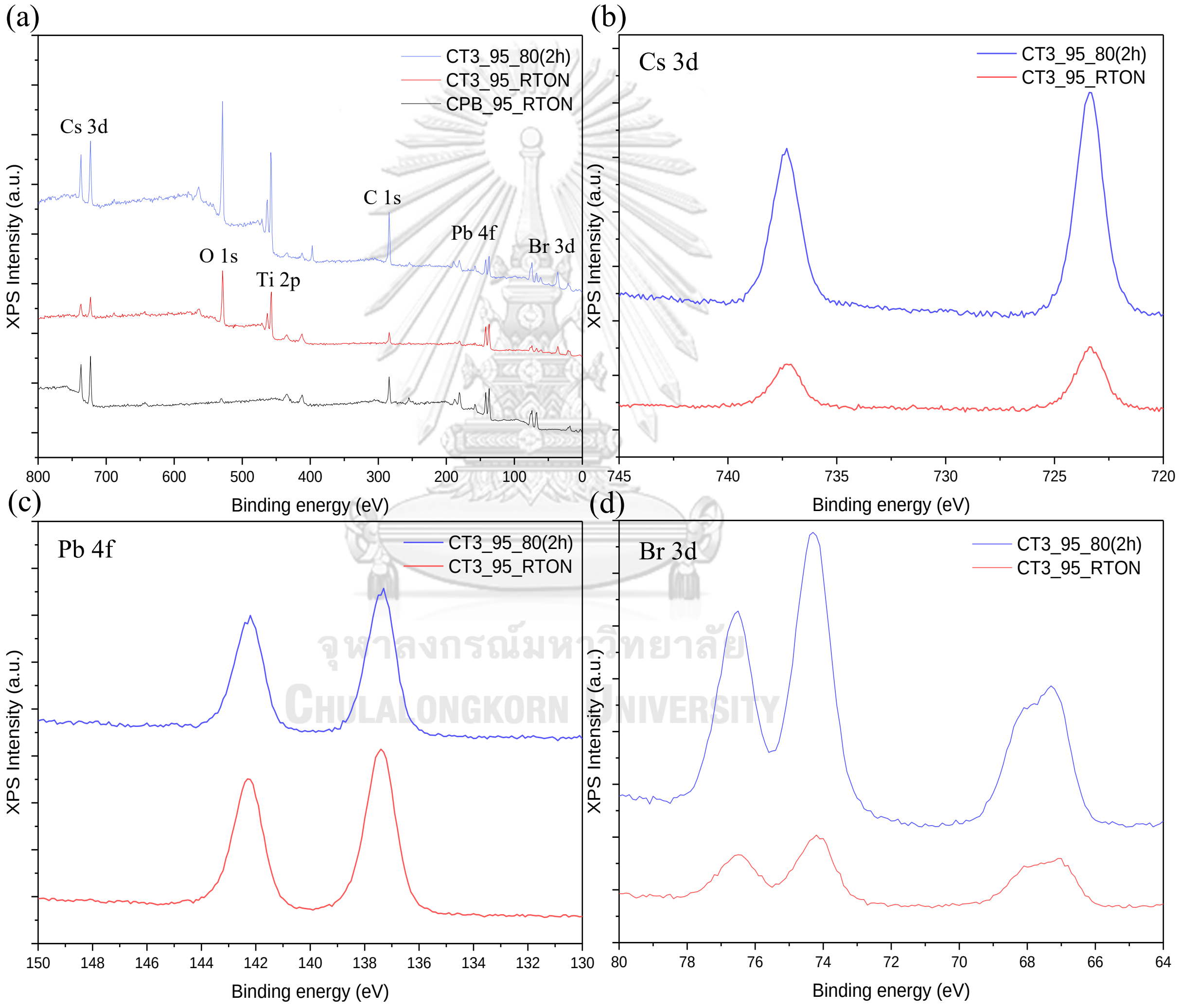

Figure 16 XPS spectra of CT3_95_80(2h), CT3_95_80ON and CPB_95_RTON and high-resolution XPS spectra of (b) Cs 3d, (c) Pb 4f, (d) Br 3d, of CT3_95_80(2h) and CT3_95_80ON composite.

4.3 Degradation of Rhodamine B

To investigate the photodegradation efficiency of $CsPbBr_3$/ Cs_4PbBr_6, visible light was used as the light source. Additionally, to confirm that the observed activity was not solely due to TiO_2, an equilibrium entry interval test was conducted. The catalysts were introduced to the equilibrium state with agitation at 250 rpm for the initial 30 min. after ultrasonic vibrations. To determine the role of TiO_2 presence, a UV light test using a 200-watt UV light source was performed. The synthesized TiO_2 was confirmed by XRD to be TiO_2 anatase, as it exhibited activity in the UV range and achieved 100% degradation within 15 min. of exposure. Comparatively, the efficiency of $CsPbBr_3/Cs_4PbBr_6$ in the visible light range was assessed by varying different parameters, as illustrated below.

From Appendix B Figure 29(a,b), it is evident that the concentration of rhodamine B solution decreases significantly during dark agitation, indicating the adsorption capability of TiO_2. Upon turning on the light, the $CsPbBr_3/Cs_4PbBr_6$ composite demonstrates its performance. Considering the wavelength of interest at 554 nm which is in visible range, anatase TiO_2 exhibits remarkable activity in the UV range. Therefore, in this photodegradation process, TiO_2 plays a crucial role in enhancing stability, likely through the agglomeration of $CsPbBr_3/Cs_4PbBr_6$ to prevent direct contact with water. From figure 17 (a,c) displays the image after normalization, clearly illustrating the initial 15 minutes following the activation of lights with the synthesis temperature was set at 95°C, the drying conditions at 80 °C for 2 h. with ratio of $CsPbBr_3/Cs_4PbBr_6$ to TBOT at 1:3, revealing an enhanced and pronounced activity during this early phase. Upon closer examination of the $\ln(C_0/C_t)$ versus time graph and the subsequent calculation results, a compelling correlation becomes apparent. The slope values derived from these experimental conditions correspond conspicuously to circumstances under which rhodamine B exhibits the most rapid photodegradation within the briefest timeframe and also owing to the larger surface area beside photoactivity after turning on the light, significant absorption is observed.

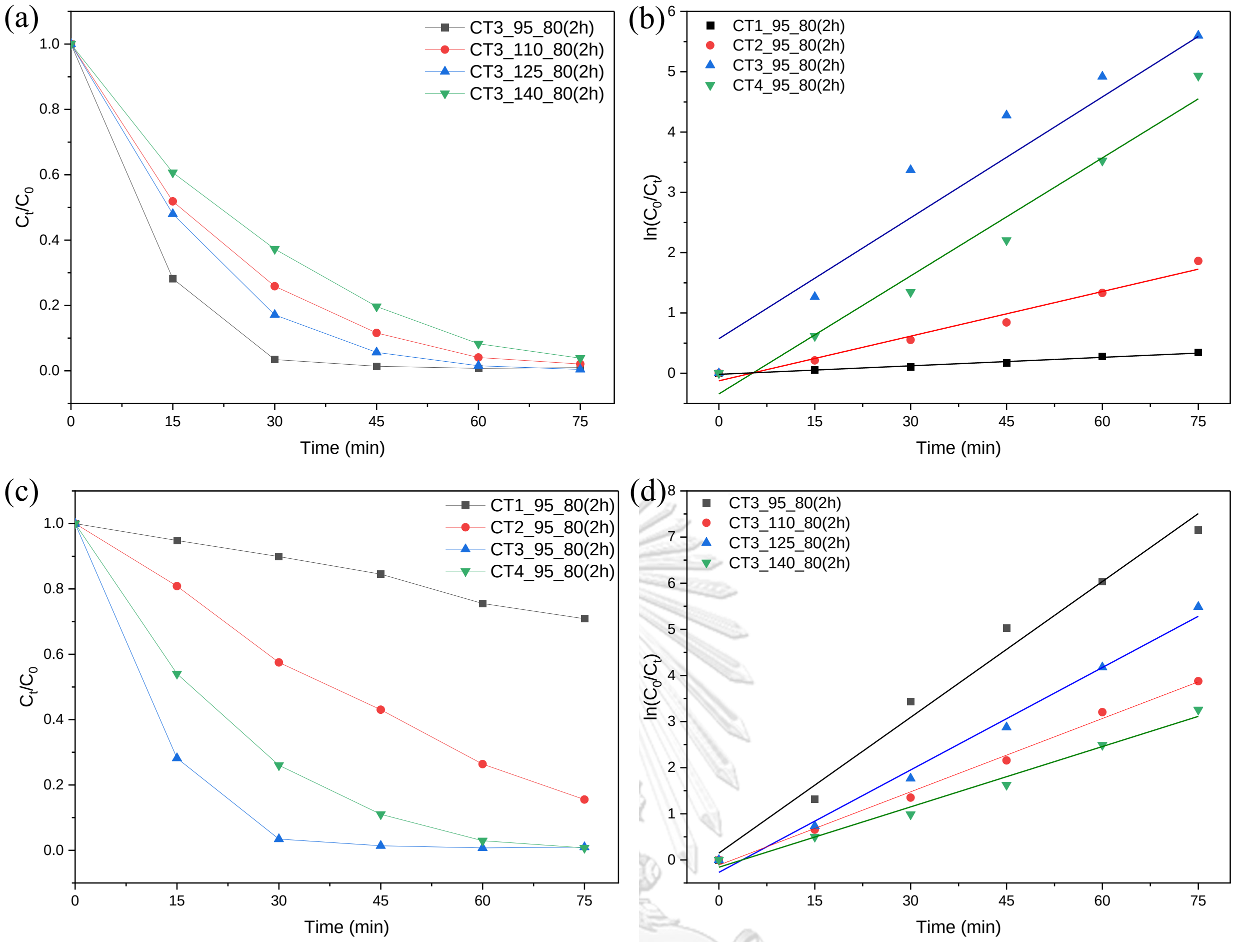

Figure 17 The normalization after turning on the light of degradation activity of Rhodamine B and fitting curves of ln (C_0/C_t) with (a,b) Different reaction temperatures and (c,d) Different vary ratios between $CsPbBr_3/Cs_4PbBr_6$ to TBOT.

From Figure 18, it is evident that the internal efficacy of Rhodamine B degradation in $CsPbBr_3/Cs_4PbBr_6$ could not be demonstrated before undergoing the one-step water-triggered transformation method with TiO_2, as it immediately lost its effectiveness upon exposure to water might be in term of the small amount of lead hydroxide which can dissolve in water as a white solid precipitate. However, this cannot be observed by naked eye but from all the results clearly show that $CsPbBr_3/Cs_4PbBr_6$ an increase in efficiency with TiO_2.

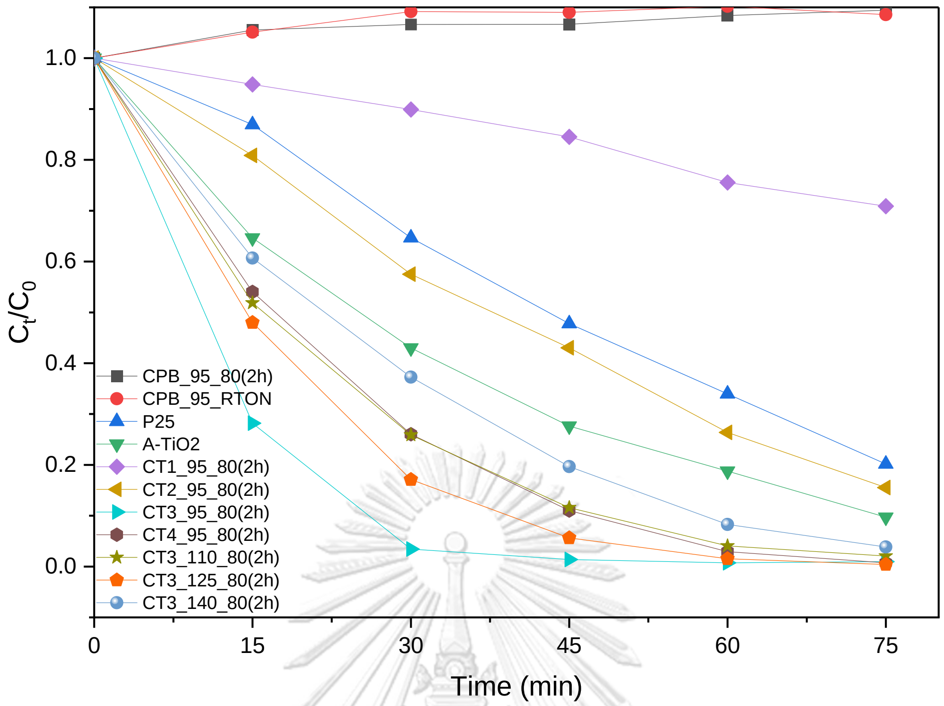

Figure 18 The overall degradation activity of Rhodamine B normalized after turning on the light.

The data regarding the photodegradation reaction of these samples can be represented using the quasi-first-order kinetic equation as $\ln(C_0/C_t) = kt$, to compare the kinetic rate constant of $CsPbBr_3/Cs_4PbBr_6$ encapsulated by TiO_2 with different conditions with commercial P25 or A-TiO_2 produced through a same process of encapsulation of $CsPbBr_3/Cs_4PbBr_6$ under visible light, the performance of $CsPbBr_3/Cs_4PbBr_6$ encapsulated by TiO_2 is superior, as indicated by the kinetic rate constants (k) values of 0.0142 min^{-1}, 0.0185 min^{-1}, and 0.1053 min^{-1} for P25, A-TiO_2, and CT3_95_80(2h), respectively. This suggests that CT3_95_80(2h) exhibits the best photocatalytic degradation performance for rhodamine B.

Table 5 Kinetic rate constants of different catalyst conditions for Rhodamine B degradation, under drying conditions at 80°C for 2 h.

Kinetic rate constant, k (min^{-1})			
Different vary ratios between $CsPbBr_3/Cs_4PbBr_6$ to TBOT		Different reaction temperatures	
CT1_95	0.0045	CT3_95	0.1053
CT2_95	0.0220	CT3_110	0.0527
CT3_95	0.0857	CT3_125	0.0699
CT4_95	0.0576	CT3_140	0.0407

It should be noted that the relationship between $CsPbBr_3/Cs_4PbBr_6$ and TiO_2 is not clearly depicted in the TEM images examined previously, as it is challenging to conclude whether TiO_2 surrounds $CsPbBr_3/Cs_4PbBr_6$ on a particle-by-particle basis. From Figure 19, the TEM images show that $CsPbBr_3/Cs_4PbBr_6$ appears to be grouped together in dark clusters, with a lighter colored area surrounding it. However, it cannot be confirmed that the surrounding boundary is TiO_2. Further investigation is needed to determine the precise heterojunction formation between these two substances which might in term of band gap heterojunction type-I or type-II, due to the larger bandgap for Cs_4PbBr_6 compared to $CsPbBr_3$, significantly increasing the exciton binding energy of the system and localizing the photogenerated carrier but the type-I bandgap model which would not only improve the PLQYs, also can lead to faster decay for $CsPbBr_3/Cs_4PbBr_6$ particle. So, as combined between $CsPbBr_3/Cs_4PbBr_6$ and TiO_2 which TiO_2 are good electron acceptors as their conduction band edge thermodynamically favors electron transfer from excited $CsPbBr_3$ and $CsPbBr_3$ acts as the middle layer, not only plays the role of electron transport, but also can capture holes, which can effectively enhance the separation of photogenerated charge carriers. These results might be able to become a type-II band arrangement which offers the best charge separation.

Chapter 5

Conclusion and Future work

5.1 Conclusion

At the synthesis temperature of 95°C with drying at 80 °C for 2 h, the highest formation of Cs_4PbBr_6 was observed, and from FTIR data revealed that the presence of Cs_4PbBr_6 improved water resistance. Additionally, when there was a mixed formation of $CsPbBr_3$ and Cs_4PbBr_6, stronger bonding and electronic interactions were observed between Cs_4PbBr_6 and the TiO_2 shell in the $CsPbBr_3/Cs_4PbBr_6$ and TiO_2 composite structure, indicating a more efficient and intimate atomic-level interaction. Examining the effect of varying ratios between $CsPbBr_3/Cs_4PbBr_6$ and TBOT, it was found that the ratio of 1:3 yielded the highest degradation efficiency within 30 min. The absorbance prior to equilibrium was the highest, and the kinetic rate constant was the highest at $k = 0.1053\ min^{-1}$, attributed to the highest BET surface area of 222 (m^2/g). The pre-equilibrium phase is attributed to the predominant absorption capacity of TiO_2. After illumination, the enhanced stabilization of TiO_2, together with the $CsPbBr_3/Cs_4PbBr_6$ structure, demonstrated clear absorbance at 554 nm within the visible light range, achieving 100% degradation within 30 min. Through the one-step water-triggered transformation method, TiO_2 greatly enhances the efficiency of pure $CsPbBr_3/Cs_4PbBr_6$ under moisture conditions. There is a possibility that the combination of $CsPbBr_3/Cs_4PbBr_6$ with TiO_2 induces complex dynamics in TiO_2. These results suggest a potential Type-II band arrangement, providing optimal charge separation with TiO_2 acting as a specialized electron acceptor. It facilitates electron transfer from the excited $CsPbBr_3$, with $CsPbBr_3$ serving as an intermediate layer that enhances the separation of light-generated charge carriers. These findings encourage further exploration for the development of the $CsPbBr_3/Cs_4PbBr_6$ system, offering potential improvements for photocatalytic applications. This enhanced degradation activity has been described in the previous chapter. But it still does not have a long life or an ability to recycle.

To assess the stability and performance of CT3_95_80(2h) after the initial round of photodegradation, a retest was conducted by separating the used catalyst from the water through centrifugation. The catalyst was then dried overnight at room temperature before repeating the test. However, the recyclable catalyst only retained 17.5% of its original net amount. Physically, the catalyst exhibited a color change from pale yellow to light pink, indicating the absorption of rhodamine B pigment. The reduction in the second pass photodegradation efficiency can be attributed to factors such as the depletion of the catalyst on the filter during absorbance. From Appendix B figure 33, the XRD pattern showed the disappearance of the $CsPbBr_3/Cs_4PbBr_6$ peak, leaving only the 2theta peak of anatase TiO_2. These results indicate a decrease in the performance of CT3_95_80(2h) after one cycle of Rhodamine B photodegradation. It is important to note that due to the significant loss of catalysts, the results of the second retest cannot be considered as conclusive or permanent data.

5.2 Future work

Although the study of $CsPbBr_3/Cs_4PbBr_6$ is still ongoing, the potential of inorganic perovskite in various conductivity and water splitting applications is increasingly captivating. However, the issue of instability in water and limited long-term stability, resulting in decreased effectiveness, needs to be addressed. Consequently, it is crucial to thoroughly investigate the water activity and duration to ensure its applicability. In the future, I aim to investigate the decomposition of pure $CsPbBr_3/Cs_4PbBr_6$ in water and identify the resultant chemical forms. Additionally, I intend to examine the nature of the relationship between $CsPbBr_3/Cs_4PbBr_6$ and TiO_2, probing the reasons behind any challenges in their recyclability. This involves scrutinizing whether the observed limitations in recyclability are attributed to an insufficient amount of recycled content. These inquiries form the foundation for future research endeavors, seeking to enhance our understanding of the interactions and recyclability aspects within the $CsPbBr_3/Cs_4PbBr_6$ and TiO_2 composite system and also find alternative methods can be explored to enhance the protection of pure

$CsPbBr_3$/Cs4PbBr$_6$ with TiO_2, apart from the one-step water-triggered transformation method. Additionally, further analysis can be conducted using various analytical tools to establish the relationship between $CsPbBr_3$/Cs_4PbBr_6 and TiO_2. It is also important to consider additional research aspects, such as examining energy bandgap, water oxidation/reduction potential levels relative to the standard hydrogen electrode (NHE) potential, and other relevant information to guide future research endeavors.

REFERENCES

[12]

VITA

NAME	Nutzeya Plainoen
DATE OF BIRTH	08 December 1997
PLACE OF BIRTH	Phatthalung, Thailand
INSTITUTIONS ATTENDED	Nutzeya Plainoen (Author) graduated from Chemical Engineering at Chulalongkorn University with a bachelor's degree in 2021 and continued the master's degree with a double degree program between Chulalongkorn University and Nation Taiwan University.
HOME ADDRESS	126/70, The best Thai-Raman, Thai-Raman Rd, Sam Wa West Sub-district, Khlong Sam Wa, Bangkok, Thailand 10510

[1] "UN's Sustainable Development Goals (SDGs) have impact on textile wastewater pollution research." https://www.newswise.com/articles/un-s-sustainable-development-goals-sdgs-have-impact-on-textile-wastewater-pollution-research (accessed April 1, 2023).

[2] S. M. Anisuzzaman, C. G. Joseph, C. K. Pang, N. A. Affandi, S. N. Maruja, and V. Vijayan, "Current Trends in the Utilization of Photolysis and Photocatalysis Treatment Processes for the Remediation of Dye Wastewater: A Short Review," *ChemEngineering,* vol. 6, no. 4, p. 58, 2022. [Online]. Available: https://www.mdpi.com/2305-7084/6/4/58.

[3] Q. Liu, "Pollution and Treatment of Dye Waste-Water," *IOP Conference Series: Earth and Environmental Science,* vol. 514, no. 5, p. 052001, 2020/05/01 2020, doi: 10.1088/1755-1315/514/5/052001.

[4] S. M. A.-A. Zumahi *et al.*, "Extraction, optical properties, and aging studies of natural pigments of various flower plants," *Heliyon,* vol. 6, 10/02 2020, doi: 10.1016/j.heliyon.2020.e05104.

[5] "Solar Radiation & Photosynthetically Active Radiation." https://www.fondriest.com/environmental-measurements/parameters/weather/photosynthetically-active-radiation/ (accessed April 1, 2023).

[6] J. Cai *et al.*, "Ion Migration in the All-Inorganic Perovskite CsPbBr3 and Its Impacts on Photodetection," *The Journal of Physical Chemistry C,* vol. 126, no. 23, pp. 10007-10013, 2022/06/16 2022, doi: 10.1021/acs.jpcc.2c03175.

[7] D. Yang, M. Cao, Q. Zhong, P. Li, X. Zhang, and Q. Zhang, "All-inorganic cesium lead halide perovskite nanocrystals: synthesis, surface engineering and applications," *Journal of Materials Chemistry C,* 10.1039/C8TC04381G vol. 7, no. 4, pp. 757-789, 2019, doi: 10.1039/C8TC04381G.

[8] A. Verma, A. P. Toor, N. T. Prakash, P. Bansal, and V. K. Sangal, "Stability and durability studies of TiO2 coated immobilized system for the degradation of

imidacloprid," *New Journal of Chemistry,* 10.1039/C7NJ00945C vol. 41, no. 14, pp. 6296-6304, 2017, doi: 10.1039/C7NJ00945C.

[9] R. Ameta, M. S. Solanki, S. Benjamin, and S. C. Ameta, "Chapter 6 - Photocatalysis," in *Advanced Oxidation Processes for Waste Water Treatment*, S. C. Ameta and R. Ameta Eds.: Academic Press, 2018, pp. 135-175.

[10] P. Kokkinos, D. Venieri, and D. Mantzavinos, "Advanced Oxidation Processes for Water and Wastewater Viral Disinfection. A Systematic Review," *Food and Environmental Virology,* vol. 13, no. 3, pp. 283-302, 2021/09/01 2021, doi: 10.1007/s12560-021-09481-1.

[11] A. Ajmal, I. Majeed, R. N. Malik, H. Idriss, and M. A. Nadeem, "Principles and mechanisms of photocatalytic dye degradation on TiO2 based photocatalysts: a comparative overview," *RSC Advances,* 10.1039/C4RA06658H vol. 4, no. 70, pp. 37003-37026, 2014, doi: 10.1039/C4RA06658H.

[12] D. Zhu and Q. Zhou, "Action and mechanism of semiconductor photocatalysis on degradation of organic pollutants in water treatment: A review," *Environmental Nanotechnology, Monitoring & Management,* vol. 12, p. 100255, 2019/12/01/ 2019, doi: https://doi.org/10.1016/j.enmm.2019.100255.

[13] A. R. Khataee and M. Fathinia, "Chapter 11 - Recent Advances in Photocatalytic Processes by Nanomaterials," in *New and Future Developments in Catalysis*, S. L. Suib Ed. Amsterdam: Elsevier, 2013, pp. 267-288.

[14] J. Jiménez Reinosa, P. Leret, C. M. Álvarez-Docio, A. del Campo, and J. F. Fernández, "Enhancement of UV absorption behavior in ZnO–TiO2 composites," *Boletín de la Sociedad Española de Cerámica y Vidrio,* vol. 55, no. 2, pp. 55-62, 2016/03/01/ 2016, doi: https://doi.org/10.1016/j.bsecv.2016.01.004.

[15] "Solar Radiation." https://www.kippzonen.com/Knowledge-Center/Theoretical-info/Solar-Radiation (accessed March 18, 2023).

[16] A. Taş, N. Cakmak, and Y. Silig, "Cytotoxicity Studies of TiO 2 /ZnO Nanocomposites on Cervical Cancer Cells," vol. 4, pp. 17-24, 12/21 2018.

[17] S. Mali, J. Patil, and C. Hong, "Simultaneous Improved Performance and Thermal Stability of Planar Metal Ion Incorporated CsPbI 2 Br All‐Inorganic Perovskite Solar Cells Based on MgZnO Nanocrystalline Electron Transporting Layer," *Advanced Energy Materials,* vol. 10, p. 1902708, 12/02 2019, doi: 10.1002/aenm.201902708.

[18] K. Tang, Y. Peng, and F. Yan, "Highly Stable All-Inorganic Perovskite Solar Cells Processed at Low Temperature," *Solar RRL,* vol. 2, p. 1800075, 05/11 2018, doi: 10.1002/solr.201800075.

[19] G. Nedelcu, L. Protesescu, S. Yakunin, M. I. Bodnarchuk, M. J. Grotevent, and M. V. Kovalenko, "Fast Anion-Exchange in Highly Luminescent Nanocrystals of Cesium Lead Halide Perovskites (CsPbX3, X = Cl, Br, I)," *Nano Letters,* vol. 15, no. 8, pp. 5635-5640, 2015/08/12 2015, doi: 10.1021/acs.nanolett.5b02404.

[20] T. G. Liashenko *et al.*, "Electronic structure of CsPbBr3−xClx perovskites: synthesis, experimental characterization, and DFT simulations," *Physical Chemistry Chemical Physics,* 10.1039/C9CP03656C vol. 21, no. 35, pp. 18930-18938, 2019, doi: 10.1039/C9CP03656C.

[21] X. Zhang *et al.*, "All-Ambient Processed Binary CsPbBr3–CsPb2Br5 Perovskites with Synergistic Enhancement for High-Efficiency Cs–Pb–Br-Based Solar Cells," *ACS Applied Materials & Interfaces,* vol. 10, no. 8, pp. 7145-7154, 2018/02/28 2018, doi: 10.1021/acsami.7b18902.

[22] M. Hussain, M. Rashid, F. Saeed, and A. Bhatti, "Spin–orbit coupling effect on energy level splitting and band structure inversion in CsPbBr3," *Journal of Materials Science,* vol. 56, pp. 1-15, 01/01 2021, doi: 10.1007/s10853-020-05298-8.

[23] X. Lu, Y. Hu, J. Guo, C.-F. Wang, and S. Chen, "Fiber‐Spinning‐Chemistry Method toward In Situ Generation of Highly Stable Halide Perovskite Nanocrystals," *Advanced Science,* vol. 6, 11/20 2019, doi: 10.1002/advs.201901694.

[24] M. He *et al.*, "CsPbBr3–Cs4PbBr6 composite nanocrystals for highly efficient pure green light emission," *Nanoscale,* 10.1039/C9NR07096F vol. 11, no. 47, pp. 22899-22906, 2019, doi: 10.1039/C9NR07096F.

[25] X. Chen *et al.*, "Centimeter-Sized Cs4PbBr6 Crystals with Embedded CsPbBr3 Nanocrystals Showing Superior Photoluminescence: Nonstoichiometry Induced Transformation and Light-Emitting Applications," *Advanced Functional Materials,* vol. 28, no. 16, p. 1706567, 2018, doi: https://doi.org/10.1002/adfm.201706567.

[26] Q. A. Akkerman *et al.*, "Nearly Monodisperse Insulator Cs4PbX6 (X = Cl, Br, I) Nanocrystals, Their Mixed Halide Compositions, and Their Transformation into CsPbX3 Nanocrystals," *Nano Letters,* vol. 17, no. 3, pp. 1924-1930, 2017/03/08 2017, doi: 10.1021/acs.nanolett.6b05262.

[27] W. Zhai *et al.*, "Solvothermal synthesis of cesium lead halide perovskite nanowires with ultra-high aspect ratios for high-performance photodetectors," *Nanoscale,* 10.1039/C8NR05683H vol. 10, no. 45, pp. 21451-21458, 2018, doi: 10.1039/C8NR05683H.

[28] F. Palazon *et al.*, "Postsynthesis Transformation of Insulating Cs(4)PbBr(6) Nanocrystals into Bright Perovskite CsPbBr(3) through Physical and Chemical Extraction of CsBr," (in eng), *ACS Energy Lett,* vol. 2, no. 10, pp. 2445-2448, Oct 13 2017, doi: 10.1021/acsenergylett.7b00842.

[29] Z. Li, L. Kong, S. Huang, and L. Li, "Highly Luminescent and Ultrastable CsPbBr3 Perovskite Quantum Dots Incorporated into a Silica/Alumina Monolith," *Angewandte Chemie International Edition,* vol. 56, no. 28, pp. 8134-8138, 2017, doi: https://doi.org/10.1002/anie.201703264.

[30] L. Bergamini, N. Sangiorgi, A. Gondolini, and A. Sanson, "CsPbBr3 for photoelectrochemical cells," *Solar Energy,* vol. 212, pp. 62-72, 2020/12/01/ 2020, doi: https://doi.org/10.1016/j.solener.2020.10.047.

[31] J. Cui *et al.*, "Facile, low-cost, and large-scale synthesis of CsPbBr3 nanorods at room-temperature with 86 % photoluminescence quantum yield," *Materials Research Bulletin,* vol. 124, p. 110731, 2020/04/01/ 2020, doi: https://doi.org/10.1016/j.materresbull.2019.110731.

[32] Z. Zhang and G. Yang, "Recent advancements in using perovskite single crystals for gamma-ray detection," *Journal of Materials Science Materials in Electronics,* 05/01 2021, doi: 10.1007/s10854-020-03519-z.

[33] S. Schünemann, M. van Gastel, and H. Tüysüz, "A CsPbBr(3) /TiO(2) Composite for Visible-Light-Driven Photocatalytic Benzyl Alcohol Oxidation," (in eng), *ChemSusChem,* vol. 11, no. 13, pp. 2057-2061, Jul 11 2018, doi: 10.1002/cssc.201800679.

[34] S. V. Deshpande *et al.*, "Rapid detoxification of polluted water using ultrastable TiO2 encapsulated CsPbBr3 QDs in collected sunlight," *Materials Research Bulletin,* vol. 142, p. 111433, 2021/10/01/ 2021, doi: https://doi.org/10.1016/j.materresbull.2021.111433.

[35] M. Imran *et al.*, "Benzoyl Halides as Alternative Precursors for the Colloidal Synthesis of Lead-Based Halide Perovskite Nanocrystals," *Journal of the American Chemical Society,* vol. 140, no. 7, pp. 2656-2664, 2018/02/21 2018, doi: 10.1021/jacs.7b13477.

[36] G. Gao *et al.*, "Novel inorganic perovskite quantum dots for photocatalysis," *Nanoscale,* 10.1039/C7NR04421F vol. 9, no. 33, pp. 12032-12038, 2017, doi: 10.1039/C7NR04421F.

[37] H. Yu *et al.*, "Green Light-Emitting Devices Based on Perovskite CsPbBr3 Quantum Dots," *Frontiers in Chemistry,* vol. 6, 08/28 2018, doi: 10.3389/fchem.2018.00381.

[38] H.-C. Wang *et al.*, "Mesoporous Silica Particles Integrated with All-Inorganic CsPbBr3 Perovskite Quantum-Dot Nanocomposites (MP-PQDs) with High Stability and Wide Color Gamut Used for Backlight Display," *Angewandte Chemie International Edition,* vol. 55, no. 28, pp. 7924-7929, 2016, doi: https://doi.org/10.1002/anie.201603698.

[39] H. Kim *et al.*, "Enhanced Optical Properties and Stability of CsPbBr3 Nanocrystals Through Nickel Doping," *Advanced Functional Materials,* vol. 31, no. 28, p. 2102770, 2021, doi: https://doi.org/10.1002/adfm.202102770.

[40] C. Meng, D. Yang, Y. Wu, X. Zhang, H. Zeng, and X. Li, "Synthesis of single CsPbBr3@SiO2 core–shell particles via surface activation," *Journal of Materials*

Chemistry C, 10.1039/D0TC03932B vol. 8, no. 48, pp. 17403-17409, 2020, doi: 10.1039/D0TC03932B.

[41] D. Takhellambam, T. R. Meena, and D. Jana, "Room temperature synthesis of blue and green emitting CsPbBr3 perovskite nanocrystals confined in mesoporous alumina film," *Chemical Communications,* 10.1039/C9CC01040H vol. 55, no. 33, pp. 4785-4788, 2019, doi: 10.1039/C9CC01040H.

[42] J. Wang, M. Li, W. Shen, W. Su, and R. He, "Ultrastable Carbon Quantum Dots-Doped MAPbBr3 Perovskite with Silica Encapsulation," *ACS Applied Materials & Interfaces,* vol. 11, no. 37, pp. 34348-34354, 2019/09/18 2019, doi: 10.1021/acsami.9b12058.

[43] J. Shen, Y. Wang, Y. Zhu, Y. Gong, and C. Li, "A polymer-coated template-confinement CsPbBr3 perovskite quantum dot composite," *Nanoscale,* 10.1039/D1NR00201E vol. 13, no. 13, pp. 6586-6591, 2021, doi: 10.1039/D1NR00201E.

[44] W. Zhu, Z. Xia, B. Shi, and C. Lü, "Water-triggered conversion of Cs4PbBr6@TiO2 into Cs4PbBr6/CsPbBr3@TiO2 three-phase heterojunction for enhanced visible-light-driven photocatalytic degradation of organic pollutants," *Materials Today Chemistry,* vol. 24, p. 100880, 2022/06/01/ 2022, doi: https://doi.org/10.1016/j.mtchem.2022.100880.

[45] O. A. Arotiba, B. O. Orimolade, and B. A. Koiki, "Visible light–driven photoelectrocatalytic semiconductor heterojunction anodes for water treatment applications," *Current Opinion in Electrochemistry,* vol. 22, pp. 25-34, 2020/08/01/ 2020, doi: https://doi.org/10.1016/j.coelec.2020.03.018.

[46] P. Verma, S. K. Samanta, and S. Mishra, "Photon-independent NaOH/H2O2—based degradation of rhodamine-B dye in aqueous medium: Kinetics, and impacts of various inorganic salts, antioxidants, and urea," *Journal of Environmental Chemical Engineering,* vol. 8, no. 4, p. 103851, 2020/08/01/ 2020, doi: https://doi.org/10.1016/j.jece.2020.103851.

[47] B. Ohtani, "Chapter 10 - Photocatalysis by inorganic solid materials: Revisiting its definition, concepts, and experimental procedures," in *Advances in*

Inorganic Chemistry, vol. 63, R. v. Eldik and G. Stochel Eds.: Academic Press, 2011, pp. 395-430.

[48] C. Zhou, Z. Liu, L. Fang, Y. Guo, Y. Feng, and M. Yang, "Kinetic and Mechanistic Study of Rhodamine B Degradation by H2O2 and Cu/Al2O3/g-C3N4 Composite," *Catalysts,* vol. 10, no. 3, p. 317, 2020. [Online]. Available: https://www.mdpi.com/2073-4344/10/3/317.

[49] "Principle of UV-Visible Spectroscopy - Detailed Explanation." https://byjus.com/chemistry/principle-of-uv-visible-spectroscopy/ (accessed April 1, 2023).

[50] "What is Photoluminescence spectroscopy?" https://www.horiba.com/ind/scientific/technologies/photoluminescence-pl/photoluminescence-pl-electroluminescence-el/ (accessed April 1, 2023).

[51] J.-G. Yu, H.-G. Yu, B. Cheng, X.-J. Zhao, J. C. Yu, and W.-K. Ho, "The Effect of Calcination Temperature on the Surface Microstructure and Photocatalytic Activity of TiO2 Thin Films Prepared by Liquid Phase Deposition," *The Journal of Physical Chemistry B,* vol. 107, no. 50, pp. 13871-13879, 2003/12/01 2003, doi: 10.1021/jp036158y.

[52] L. Jing, F. Yuan, H. Hou, B. Xin, W. Cai, and H. Fu, "Relationships of surface oxygen vacancies with photoluminescence and photocatalytic performance of ZnO nanoparticles," *Science in China Series B: Chemistry,* vol. 48, no. 1, pp. 25-30, 2005/01/01 2005, doi: 10.1007/BF02990909.

[53] "X-ray Powder Diffraction (XRD)." https://serc.carleton.edu/research_education/geochemsheets/techniques/XRD.html (accessed April 1, 2023).

[54] M. Kannan, "Scanning Electron Microscopy: Principle, Components and Applications," 2018, pp. 81-92.

[55] C. B. C. David B. Williams "Transmission Electron Microscopy," 2009, pp. 3-22.

[56] C. Berthomieu and R. Hienerwadel, "Fourier transform infrared (FTIR) spectroscopy," *Photosynthesis research,* vol. 101, pp. 157-70, 07/01 2009, doi: 10.1007/s11120-009-9439-x.

[57] S. d. Silva, C. Braga, M. Fook, C. Raposo, L. Carvalho, and E. Canedo, "Application of Infrared Spectroscopy to Analysis of Chitosan/Clay Nanocomposites," 2012, p. (22 pp).

[58] S. Daniel, "Chapter 4 - Characterization of carbon dots," in *Carbon Dots in Analytical Chemistry*, S. K. Kailasa and C. M. Hussain Eds.: Elsevier, 2023, pp. 43-58.

[59] A. Fahlman, C. Nordling, and K. Siegbahn, *ESCA : atomic, molecular and solid state structure studied by means of electron spectroscopy*. Uppsala : Almqvist and Wiksell (in eng), 1967.

[60] "BET Theory." https://wiki.anton-paar.com/en/bet-theory/ (accessed March 18, 2023).

[61] M. Wang, Q. Yu, T. Yu, S. Zhang, M. Gong, and Y. Liu, "Manipulating the formation of cesium lead bromide nanocrystals via oleic acid," *RSC Advances,* 10.1039/D2RA06491J vol. 13, no. 8, pp. 5158-5167, 2023, doi: 10.1039/D2RA06491J.

[62] J. H. Heo, J. K. Park, and S. H. Im, "Full-Color Spectrum Coverage by High-Color-Purity Perovskite Nanocrystal Light-Emitting Diodes," *Cell Reports Physical Science,* vol. 1, no. 9, p. 100177, 2020/09/23/ 2020, doi: https://doi.org/10.1016/j.xcrp.2020.100177.

[63] L. Yang *et al.*, "A P25/(NH4)xWO3 hybrid photocatalyst with broad spectrum photocatalytic properties under UV, visible, and near-infrared irradiation," *Scientific Reports,* vol. 8, p. 45715, 04/01 2017, doi: 10.1038/srep45715.

Appendix A

Appendix A Raw data

A.1 The degradation activity of Rhodamine B of pure $CsPbBr_3/Cs_4PbBr_6$

A.1.1 At reaction temperature of 95°C with drying at 80 °C for 2 h

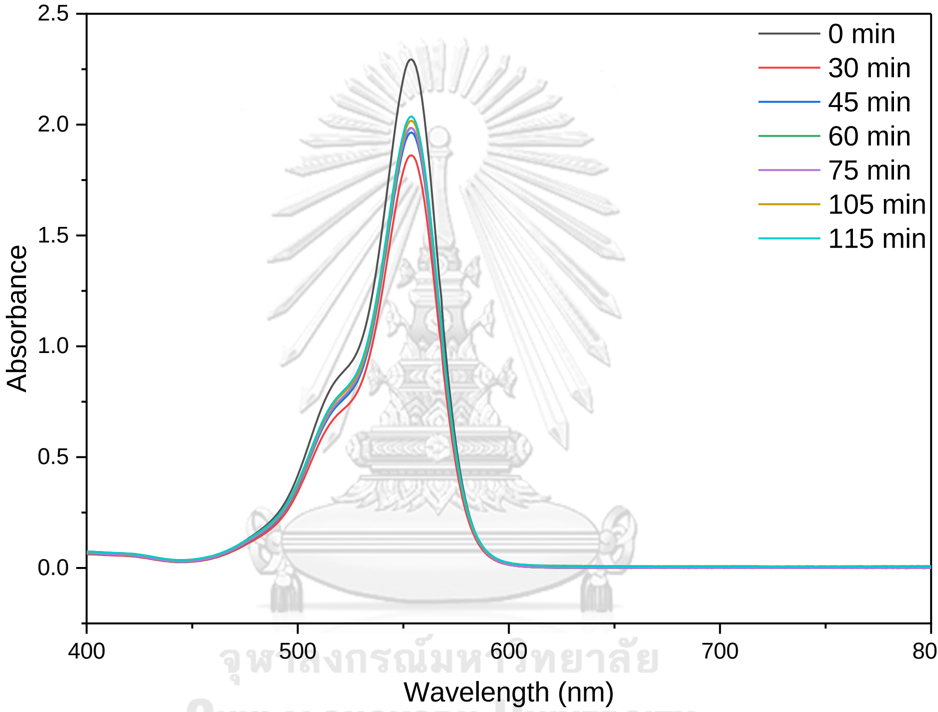

Figure 19 The degradation activity of Rhodamine B of pure $CsPbBr_3/Cs_4PbBr_6$ at reaction temperature of 95°C with drying at 80 °C for 2 h.

A.2 The degradation activity of Rhodamine B of $CsPbBr_3/Cs_4PbBr_6$ and TiO_2

A.2.1 At vary the reaction temperature with drying at 80 °C for 2 h.

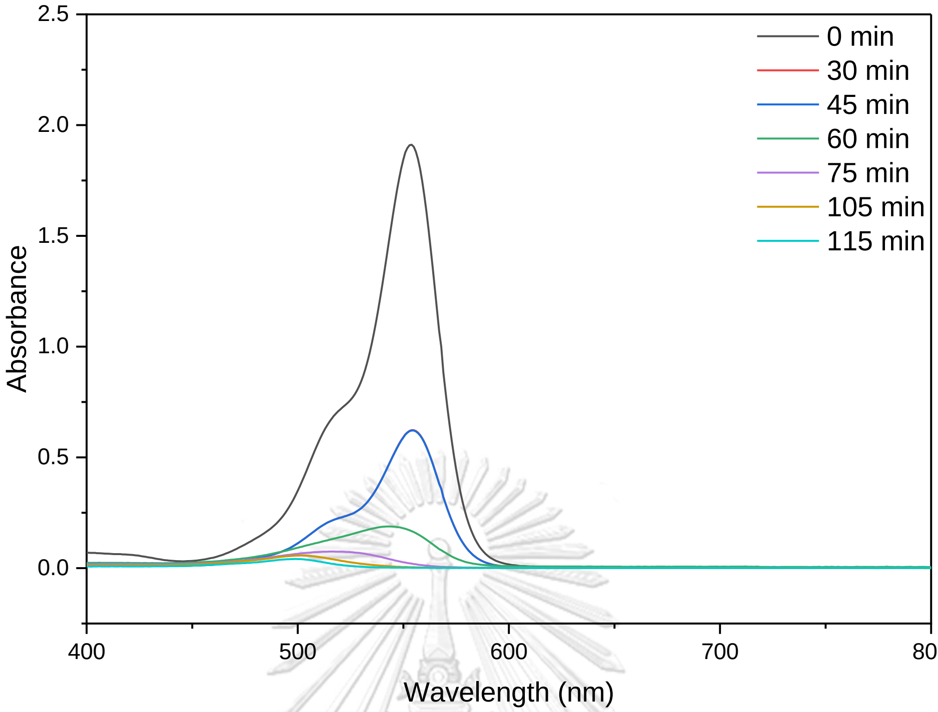

Figure 20 The degradation activity of Rhodamine B at reaction temperature of 95°C.

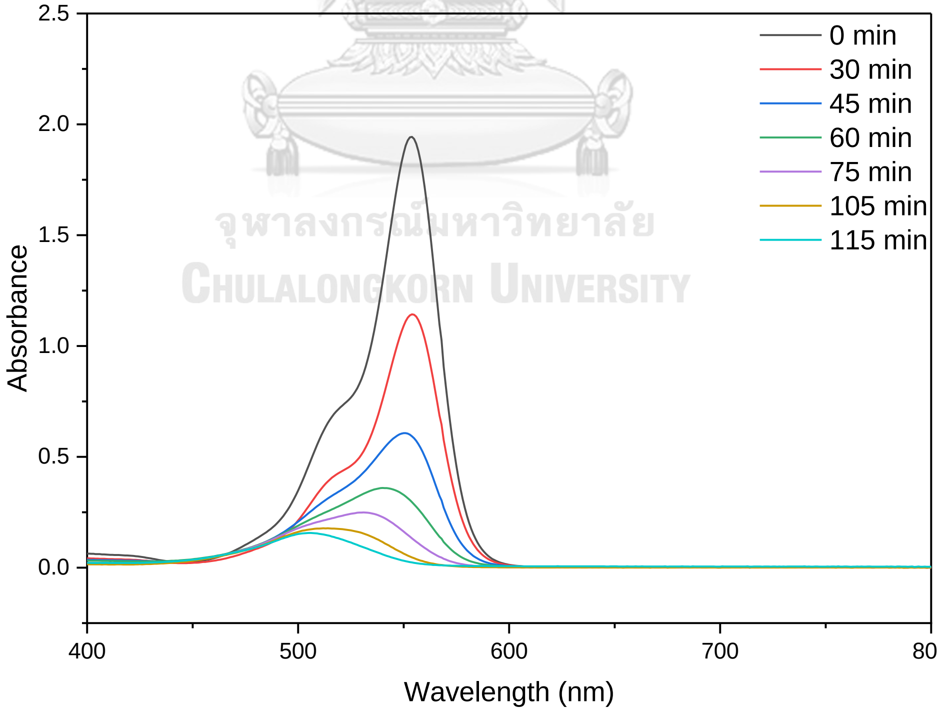

Figure 21 The degradation activity of Rhodamine B at reaction temperature of 110°C.

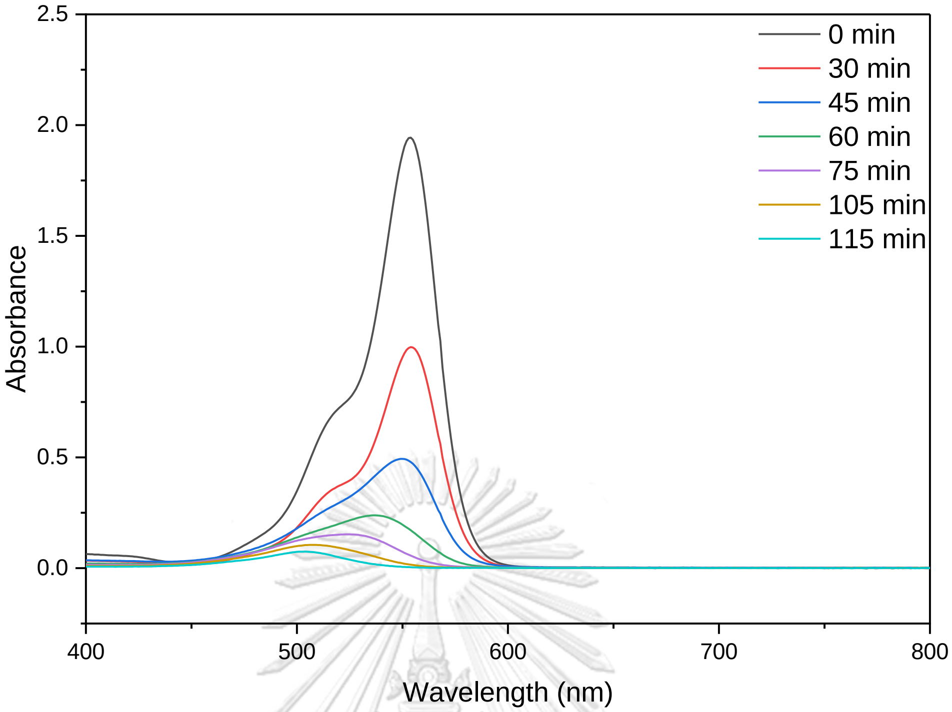

Figure 22 The degradation activity of Rhodamine B at reaction temperature of 125°C.

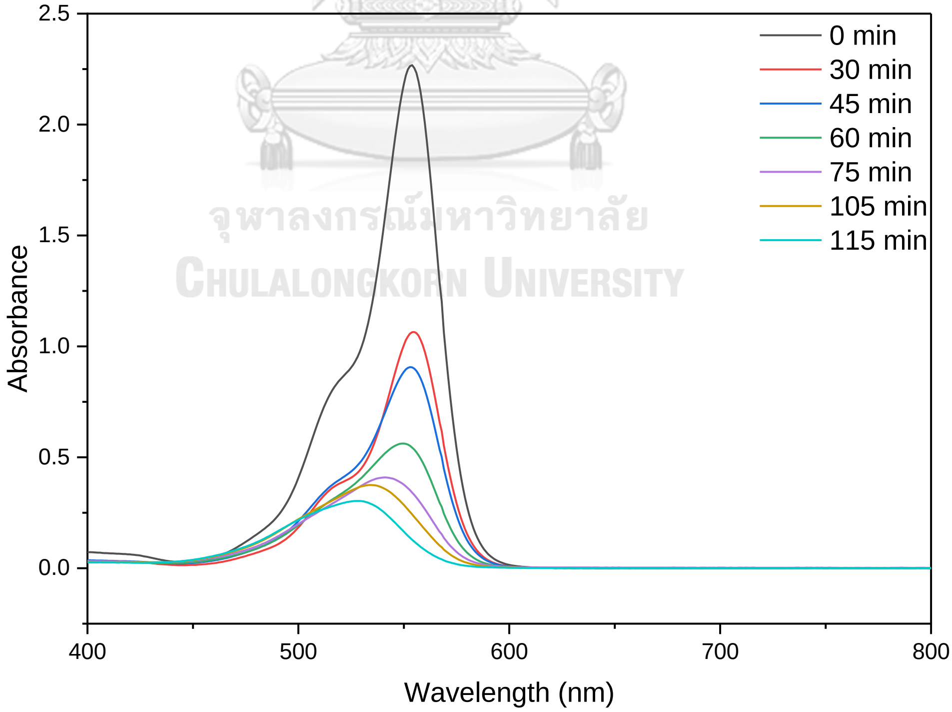

Figure 23 The degradation activity of Rhodamine B at reaction temperature of 140°C.

A.2.2 At vary ration reaction between $CsPbBr_3/Cs_4PbBr_6$ and TiO_2 with reaction temperature of 95°C, drying at 80 °C for 2 h.

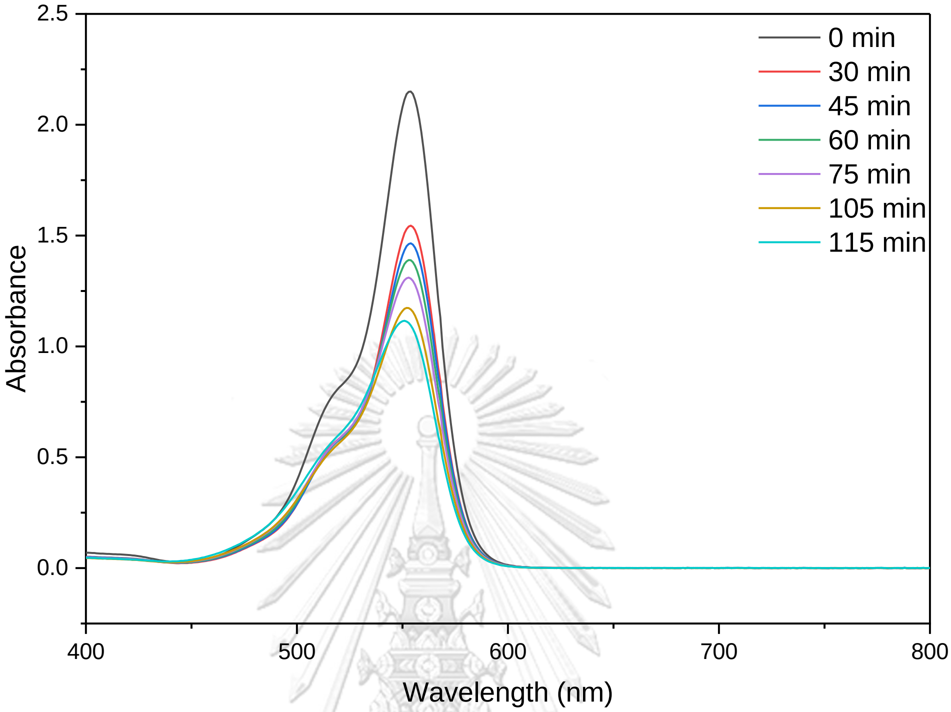

Figure 24 The degradation activity of Rhodamine B with ratio between $CsPbBr_3/Cs_4PbBr_6$ to TBOT is 1:1.

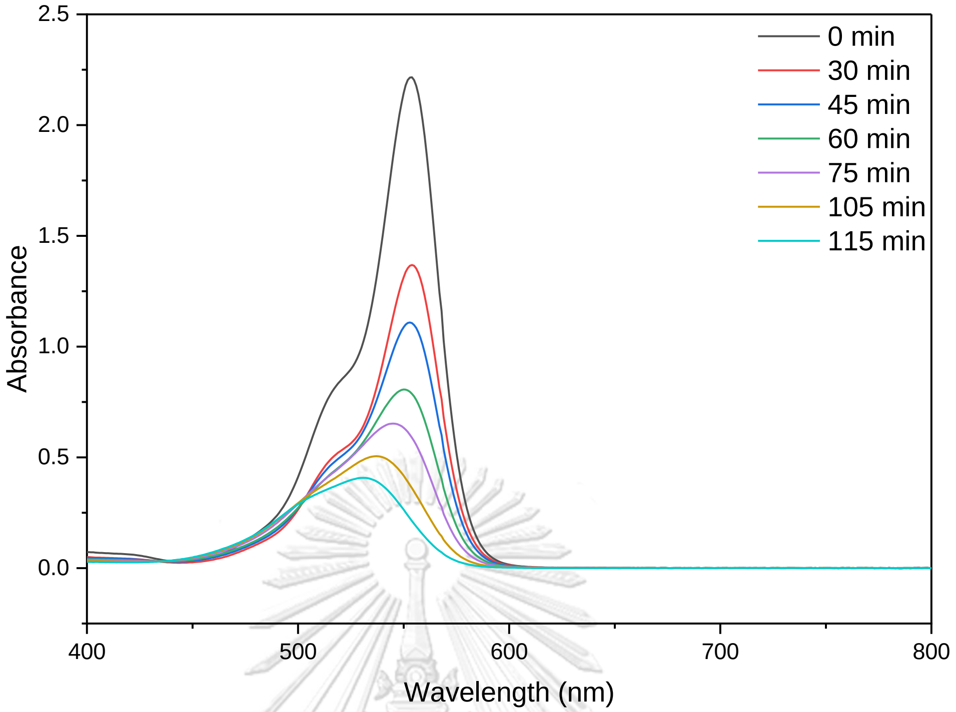

Figure 25 The degradation activity of Rhodamine B with ratio between $CsPbBr_3/Cs_4PbBr_6$ to TBOT is 1:2.

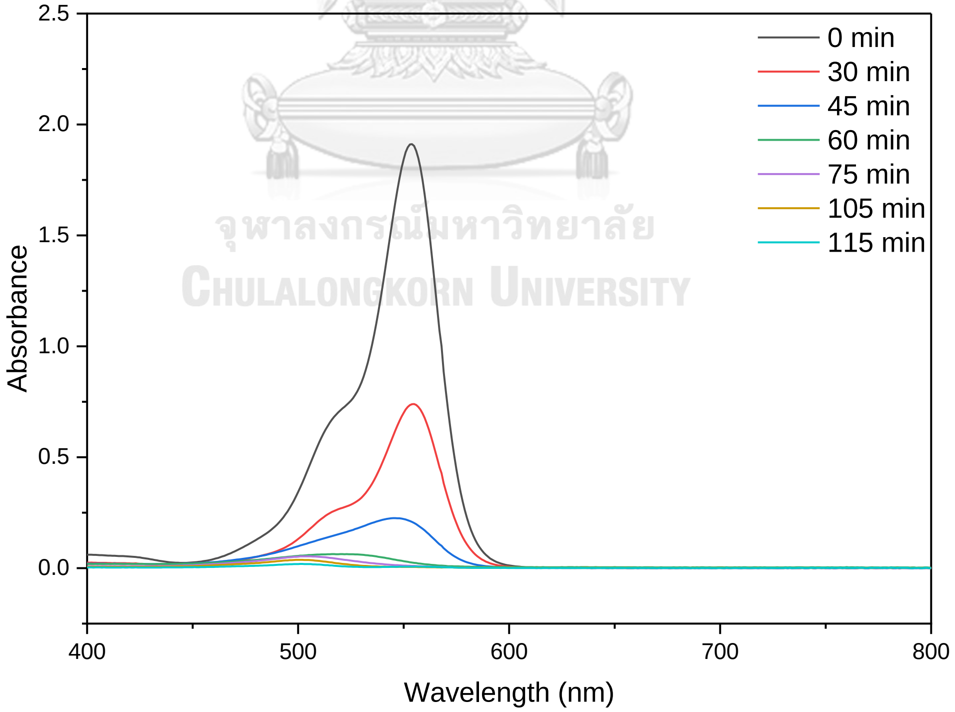

Figure 26 The degradation activity of Rhodamine B with ratio between $CsPbBr_3/Cs_4PbBr_6$ to TBOT is 1:3.

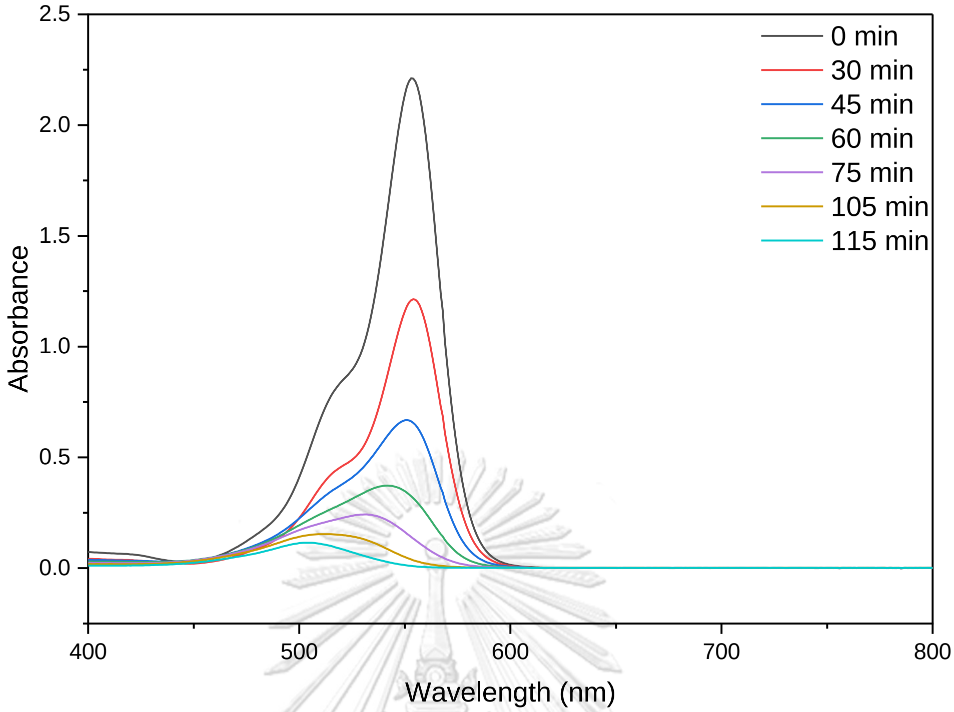

Figure 27 The degradation activity of Rhodamine B with ratio between $CsPbBr_3/Cs_4PbBr_6$ to TBOT is 1:4.

A.3 The degradation activity of Rhodamine B of P25

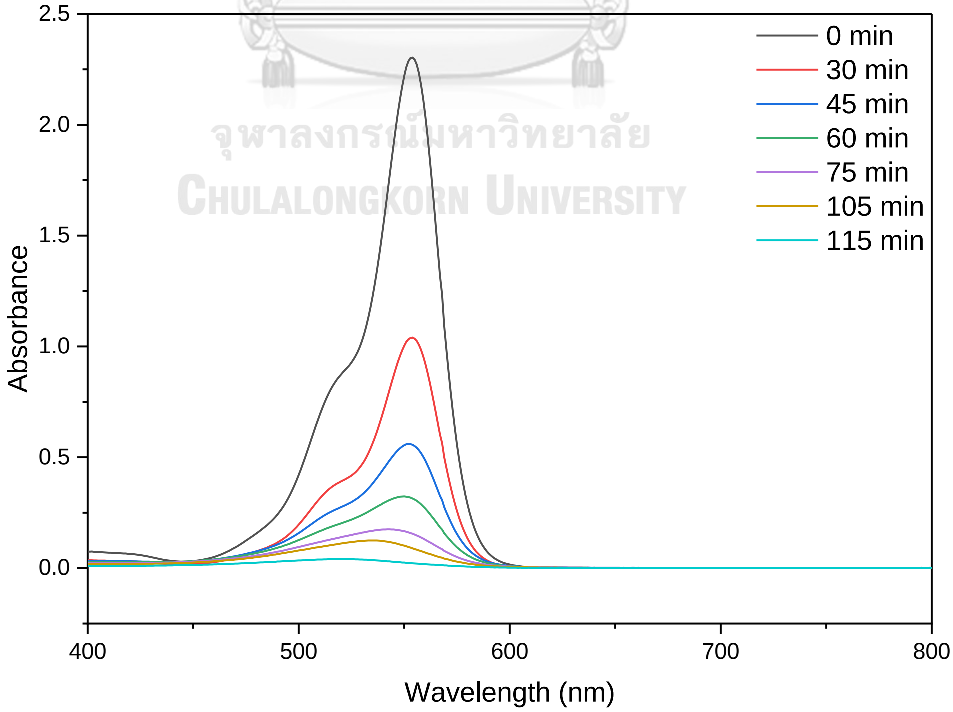

Figure 28 The degradation activity of Rhodamine B with P25.

Appendix B

Appendix B Characteristics of catalysts

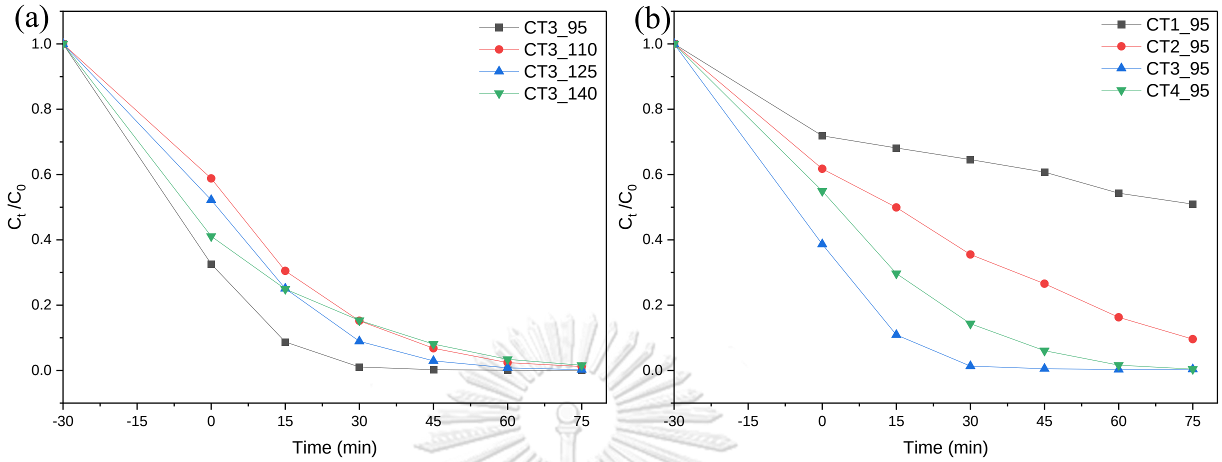

Figure 29 The degradation activity of Rhodamine B with (a) Different reaction temperatures and (b) Different vary ratios between $CsPbBr_3/Cs_4PbBr_6$ to TBOT.

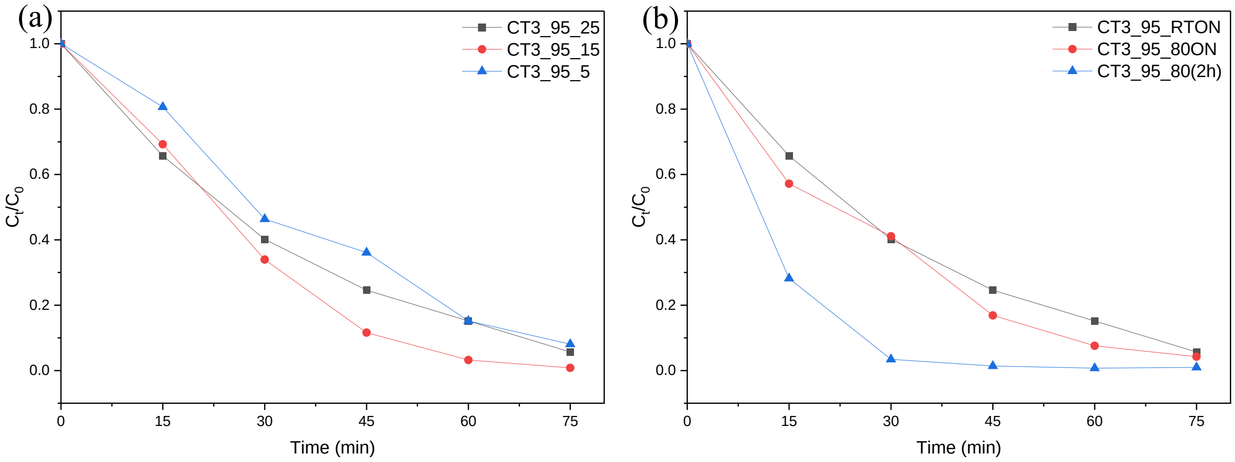

Figure 30 The normalization after turning on the light of degradation activity of Rhodamine B with (a) Different amount of water and (b) Different drying conditions.

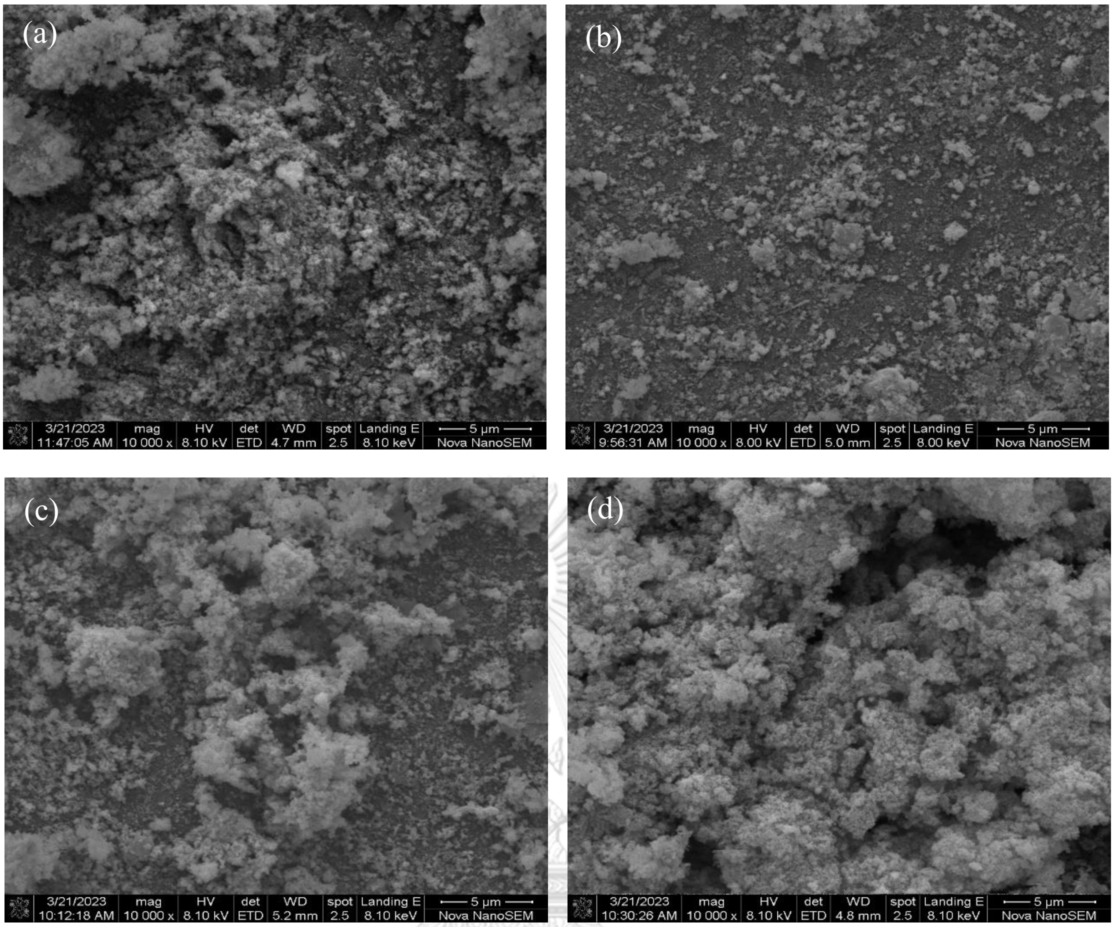

Figure 31 SEM images of $CsPbBr_3/Cs_4PbBr_6$ encapsulated by TiO_2 at ratio between $CsPbBr_3/Cs_4PbBr_6$ to TBOT is 1:3 with different reaction temperature (a) 95°C and (b) 110°C and (c) 125°C and (d) 140°C.

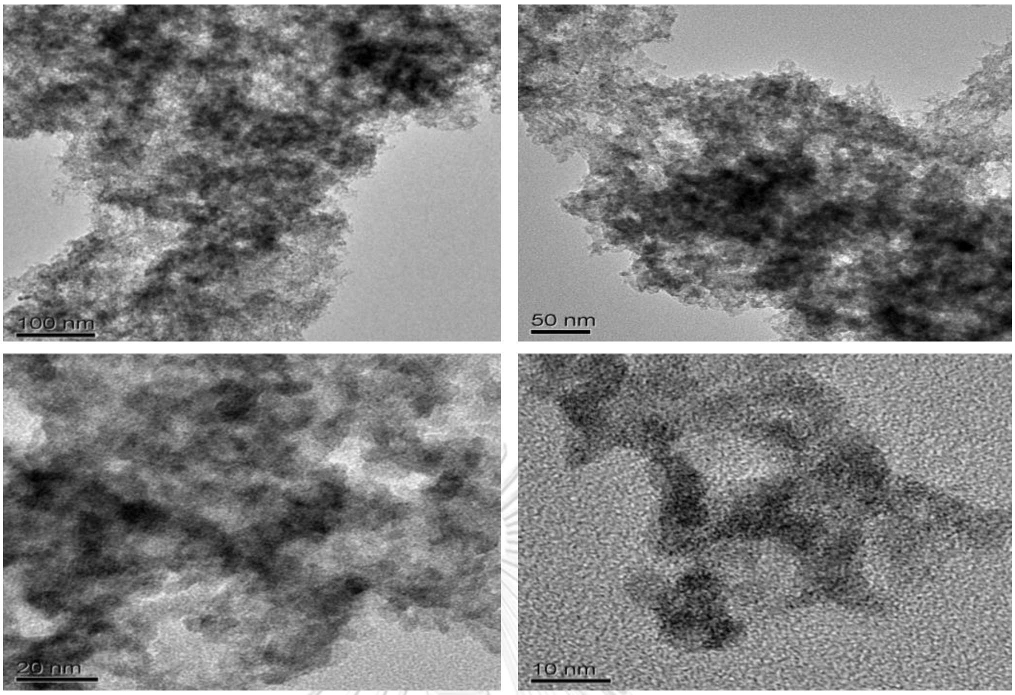

Figure 32 TEM images of $CsPbBr_3/Cs_4PbBr_6$ encapsulated by TiO_2 at 95°C prepared at the mass ratio between $CsPbBr_3/Cs_4PbBr_6$ to TBOT is 1:3.

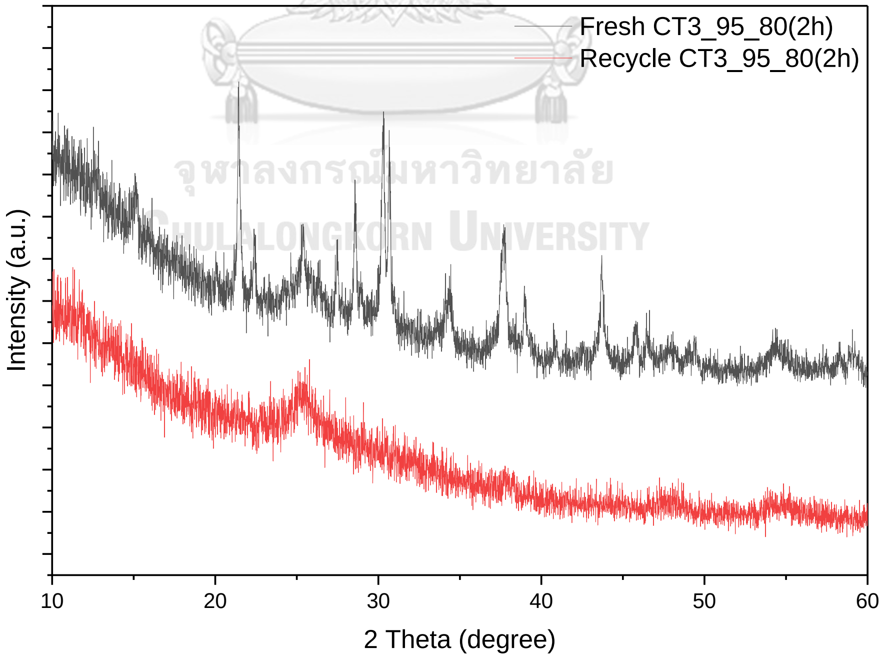

Figure 33 XRD patterns of $CsPbBr_3/Cs_4PbBr_6$ encapsulated by TiO_2 at 95°C (a) before and (b) after one cycle of photodegradation.